SiO Maser Survey of Cold IRAS Sources

Jun-ichi Nakashima*

Department of Astronomical Science, The Graduate University for Advanced Studies, Nobeyama Radio Observatory, Minamimaki, Minamisaku, Nagano 384-1305 junichi@astro.uiuc.edu

and

Shuji Deguchi

Nobeyama Radio Observatory, National Astronomical Observatory,
Minamimaki, Minamisaku, Nagano 384-1305
dequchi@nro.nao.ac.jp

(Received 2002 August 22; accepted 2002 November 16)

Abstract

We present the results of observations of cold IRAS sources in the Galactic disk area, $-10^{\circ} < l < 100^{\circ}$ and $|b| < 5^{\circ}$, in the SiO J = 1-0, v = 1 and 2 maser lines. SiO masers were detected in 51 out of 143 observed sources; 45 were new detections in SiO masers. The selected IRAS sources were objects with dust temperatures of between 160 and 280 K. According to a confirmation using 2MASS near-infrared images, a majority of the sample are AGB or post-AGB stars, although dense cores in the starforming regions (or dusty HII regions) are involved in part of the sample. Among new detections, two were candidates for post-AGB stars: IRAS 18450-0148 (W 43A), and 19312+1950. We found that the intensity ratios of the SiO J=1-0, v=2 to the v=1 line of the objects clearly correlate with those IRAS colors. The detection rates of SiO masers tend to increase toward the Galactic center as well as the cases of previous SiO maser surveys of typical AGB stars. No strong associations of the objects to the spiral arms were found. The radial-velocity dispersion of the present sample is comparable with the dispersion of the SiO maser sample of typical AGB stars. These facts suggest that the present sample of cold IRAS sources with SiO masers has a kinematic property very similar with that of typical AGB stars.

Key words: Stars: late-type — masers — Stars: AGB and post-AGB — Galaxy: kinematics and dynamics

^{*} Present address: Department of Astronomy, University of Illinois at Urbana-Champaign, 1002 West Green Street, MC-221, Urbana, IL 61801

1. Introduction

A sample of cold IRAS point sources mainly consists of evolved stellar objects with a thick dusty envelope (David et al. 1993; Likkel et al. 1987; Likkel 1989; Likkel et al. 1991; Silva et al. 1993; te Lintel Hekkert 1991a), young stellar objects in star-forming regions, and dusty HII regions accompanying hot stars (Pashchenko, Le Skeren 1994; Wilking et al. 1989, 1990; Yang et al. 2002). Because both late-type stellar objects and young stellar objects exhibit similar IRAS colors, it is difficult to distinguish the evolved stars from young stellar objects solely from the IRAS color indices (e.g., van der Veen et al. 1989). In addition, because considerable percentages of the IRAS 60 μ m flux densities of the bulge AGB stars near the galactic plane were found to be contaminated by dust emission from surrounding interstellar clouds (Izumiura et al. 1999; Deguchi et al. 2000a, b), the color index, C_{23} (a logarithmic ratio of IRAS 60 to 25 μ m flux density), may not effectively used to identify the late-type stellar objects (AGB or post-AGB stars) among these cold objects. Mass-losing O-rich AGB stars very often exhibit maser emission; OH (1612 MHz) and H₂O maser lines have been used to identify evolved stellar objects among cold IRAS sources (David et al. 1993; Likkel 1989; Silva et al. 1993; te Lintel Hekkert 1991a). SiO masers could also be an identifier of late-type stellar objects. However, it has been found in the past SiO maser surveys that the detection rate of SiO masers are maximized at the IRAS color, $C_{12} \simeq 0$ ($T_{\rm dust} \simeq 300$ K; C_{12} , a logarithmic ratio of IRAS 25 to 12 μ m flux densities) and the rate drops quickly in $C_{12} > 0.2$ ($C_{12} = 0.2$ corresponds to $T_{\rm dust} \simeq 280 {\rm K};$ e.g., Jiang et al. 1995; Nyman et al. 1998). Therefore, for IRAS objects with $C_{12} > 0.3$, SiO maser surveys have never been rigorously conducted at Nobeyama.

In the IRAS two-color diagram (e.g., van der Veen, Habing 1988), typical mass-losing AGB stars occupy the region $C_{12} < 0.4$ and $C_{23} < -0.1$ (region III in figure 2 in van der Veen, Breukers 1989). More evolved objects with thicker/hollow dust shells fall in the region $C_{12} > 0.4$ or $C_{23} > -0.1$ (regions IV and VIII). The boundary between the AGB and the post-AGB phase (proto-planetary nebula phase) is considered to lie around $C_{12} \simeq 0.5$ (e.g., Nyman et al. 1998; van der Veen, Habing 1988). Therefore, the cold IRAS objects with SiO masers ($C_{12} \gtrsim 0.5$) are stars with a very thick dust shell, which are at a very late stage of the AGB phase (or possibly at a very early post-AGB phase).

Proto-planetary nebulae are transient objects between the AGB phase and planetary nebulae. These objects often have colors beyond $C_{12} \sim 0.5$. Detections of SiO masers from such objects must indicate that they are at a very early phase of proto-planetary nebulae, objects of decreasing mass-loss rate, developing a high-velocity flow, and creating a hollow dust shell (Engels 2002). Such objects occasionally appear as large extended nebulae (the apparent size is larger than $\sim 10''$) in the near-infrared, as, for example, OH 231.8+1.4 (Morris et al. 1987) and IRAS 19312+1950 (Nakashima, Deguchi 2000). However, not all of the objects with colors beyond $C_{12} \sim 0.5$ exhibit such large extended nebulosity. It is rather relatively rare to find

such well-developed nebulous objects like as OH231.8+1.4 in near- and mid-infrared imaging surveys (e.g., Meixner et al. 1999).

An alternative idea (Suh, Jones 1997) to explain the SiO masers in cold IRAS sources is that these objects with high C_{12} are still at the AGB phase, and are at periods soon after a He-shell flash in a super-wind phase when a central star temporarily decreases or terminates the mass-loss (e.g., Vassiliadis, Wood 1993; Blöcker 1995). Because of the highly reddened colors ($C_{12} \gtrsim 0.5$), these objects must be at a phase nearly leaving AGB (but still in O-rich; e.g., van Loon et al. 2001). A temporal termination of mass-loss creates a hollow shell which exhibits a high C_{12} color. A gradual recovery of mass-loss after the He-shell flash restarts SiO masers, which are emitted near the central star within a few stellar radii. These objects may mimic the colors of post-AGB stars, but may not have extended nebulosity.

In order to find more SiO masers in cold IRAS sources and to investigate their properties, we surveyed cold IRAS objects with $T_{\rm dust}=160$ –280 K near the galactic plane in 43 GHz SiO maser lines. The outline of the paper is as follows. In section 2, we describe the source selection, the observation, the data reduction and the results of observations. In section 3, we discuss the color characteristics of SiO detections, the intensity ratio of the J=1–0, v=2 to v=1 line and the longitude distribution of the detections. In section 4, we discuss remarkable individual objects in the sample, and finally conclude the paper in section 5.

2. Observations

2.1. Source Selection

The present sample was selected from the IRAS Point Source Catalog (version 2) in the area of the Galactic plane, $-10^{\circ} < l < 100^{\circ}$, and $|b| < 5^{\circ}$ (with one exception, IRAS 23572+6702, see table 1). The selected color ranges were $0.2 < C_{12} \equiv \log(F_{25}/F_{12}) < 0.8$, and $-1.0 < C_{23} \equiv \log(F_{60}/F_{25}) < 1.5$, where F_{12} , F_{25} , and F_{60} are IRAS 12, 25, and 60 μ m flux densities, respectively. These color criteria effectively extract dust-enshrouded objects with $T_{\rm duxt} \simeq 160$ –280 K. The total number of observed sources was 143. Figure 1 shows the distribution of the observed sources in the Galactic coordinates. The IRAS 12 μ m flux densities of observed sources range from about 2 Jy to over 1000 Jy, and most of the observed sources are brighter than 10 Jy at 12 μ m.

Near-infrared imaging observations of IRAS / SiO sources at the inner disk (Deguchi et al. 2001a) confirmed that a considerable number of near-infrared counterparts are located at positions with large angular separations (more than 10") from the IRAS positions. Because of the high source density in the Galactic disk and bulge, the IRAS satellite might not determine the positions well, and the IRAS positions may not be sufficient to place faint mid-infrared sources in a telescope beam. Therefore, we partly used the positions in the MSX catalog instead of those in the IRAS catalog (MSX: Midcourse Space Experiment; Price et al. 1997).

Since the typical astrometric uncertainty of positions in the MSX catalog is a few arcsec, it is sufficient to place mid-infrared point sources in the telescope beam of HPBW= 40" for the present SiO observations. We crosschecked the source positions between the IRAS and MSX catalogs, and adopted the positions of the MSX sources nearest to the IRAS positions within 40" as a counterpart. The adopted MSX counterparts and the angular separation from the IRAS positions are given in table 1. We found that only three MSX counterparts have large separations (more than 20") from the IRAS positions. Figure 2 shows a comparison of the flux densities between the corresponding IRAS and MSX sources, and figure 3 is the same plot for mid-infrared colors. Because the MSX fluxes and colors correlate well with those of IRAS, most of the identifications are considered to be made correctly. However, because most of the sources in the present sample are Mira-type pulsating stars (e.g., Nakashima et al. 2000), the sample in figures 2 and 3 has a moderate dispersion, as expected from time variations of ~ 0.5 mag at mid-infrared wavelengths (e.g., Onaka et al. 1997). In fact, because the MSX catalog became available around May 2000 when we had finished the survey of 90 sources at $l > 40^{\circ}$, we used the MSX positions for the survey of 53 sources at $-10^{\circ} < l < 40^{\circ}$. Therefore, we list in table 1 the MSX counterparts of IRAS sources only for the sources at $-10^{\circ} < l < 40^{\circ}$.

2.2. Observations and Results

Simultaneous observations in the SiO J = 1-0, v = 1 and 2 transitions at 43.122 and 42.821 GHz, respectively, were made with the 45-m radio telescope at Nobeyama during the periods of 2000 April-May and 2001 March. In addition to the SiO lines, observations in the H_2O , 6(1,6)-5(2,3) transition at 22.235 GHz were made for the SiO maser emitters, which were found during the present SiO observations. The beam size of the telescope was about 40" at 43 GHz and 72" at 22 GHz. In the SiO observations, a cooled SIS receiver with a bandwidth of about 0.4 GHz was used, and the system noise temperatures (including atmospheric noise and antenna ohmic loss) were about 200–300 K (SSB), depending on the weather conditions. In the H₂O observations, a cooled HEMT receiver with a bandwidth of about 2 GHz was used, and the system noise temperatures were about 170–300 K. The aperture efficiency of the telescope was about 0.57 at 43 GHz and 0.62 at 22 GHz. The conversion factor from the antenna temperature to the flux density was 2.9 Jy K^{-1} at 43 GHz and 3.0 Jy K^{-1} at 22 GHz. Acoustooptical spectrometer arrays of high and low resolutions (AOS-H and AOS-W) were used. The AOS-H spectrometer has a 40 MHz bandwidth and 2048 frequency channels, with an effective spectral resolution of 0.29 km s⁻¹ at 43 GHz and 0.50 km s⁻¹ at 22 GHz. Likewise, the AOS-W spectrometer has a 250MHz bandwidth and 2048 frequency channels, with an effective spectral resolution of 1.7 km s⁻¹ at 43 GHz and 3.4 km s⁻¹ at 22 GHz. We used multiple AOS-H spectrometers to cover a wide velocity range at a high frequency resolution. Because the line widths of masers are often less than 1 km s⁻¹, we need the high resolution achieved by the AOS-H. The radial-velocity coverage was $\pm 350 \text{ km s}^{-1}$ at 43 GHz and $\pm 600 \text{ km s}^{-1}$ at 22

GHz. This entire velocity range was covered by the AOS-H spectrometers (AOS-W was used to confirm the detections). All of the observations were made in position-switching mode using 10' off-positions at both 43 and 22 GHz. The pointing accuracy of the telescope was checked every 2 or 3 hours by 5-point mapping of nearby SiO maser sources, V1111 Oph and χ Cyg. The pointing accuracy was found to be better than 5".

Raw data were processed by flagging out bad scans, making r.m.s.-weighted integrations, and removing slopes in the baselines. Detections of maser lines were judged by the following criteria. For narrow spike-type emissions, the peak antenna temperature must be greater than the 3 σ level of the r.m.s. noise. (For extremely narrow lines with a bandwidth less than 1 km s⁻¹, we carefully checked individual scans in raw data to exclude spurious lines.) For broad emissions, the effective signal-to-noise ratio (S/N) over the line width must be larger than 10; the effective S/N was calculated from integrated intensities and the r.m.s. noise. Furthermore, we inspected each spectrum by eye and discarded some marginal detection that satisfied the above criteria.

Finally, we obtained 51 detections out of 143 observed sources in either SiO J=1-0, v=1 or 2 transitions; 45 of 51 detected sources were new detections in SiO masers, and 9 of 45 new detections had never been detected in OH or H_2O maser lines. The results of our observations of SiO masers are summarized in table 2 for detections and in table 3 for non-detections. The spectra of the detections are shown in figure 4. The velocities, V_{lsr} , in table 2 are the radial velocities at the intensity peaks of spectra of SiO masers. In the case of the H_2O maser line, we detected 3 out of 23 observed sources; only one of them (IRAS 19312+1950) was a new detection in the H_2O maser line (e.g., Nakashima, Deguchi 2000). The H_2O maser spectra are shown in figure 5. All of the detected H_2O masers were recognized as "Type B" profiles (double peak; e.g., Engels et al. 1986). At first glance, the H_2O maser of IRAS 19312+1950 (see figure 1 in Nakashima, Deguchi 2000) seems to be like "Type A" (single peak at the stellar velocity), but should be regarded as "Type B", because we confirmed the other velocity component at $V_{lsr} \sim 60 \text{ km s}^{-1}$ by a recent observation (Deguchi and Nakashima, in preparation). The line parameters are summarized in table 4 for H_2O detections. The results of non-detections are listed in table 5.

3. Statistical Properties and Discussions

3.1. Color Characteristics of SiO Detections

Figure 6 shows a two-color diagram of the observed sources. The broken lines in figure 6 indicate the boundaries of the source types suggested by van der Veen, Habing (1988). The observed sources distribute mostly in regions IIIb, IV, and VIII, which are mainly composed of variable AGB stars with thick O-rich circumstellar shells, variable AGB stars with very thick O-rich circumstellar shells, and other kinds of very cool objects, respectively (van der

Veen, Habing 1988). SiO detections clearly concentrate into the regions IIIb and IV. This phenomenon supports previous findings that SiO masers are emitted mostly from AGB stars with an O-rich dust envelope (e.g., Habing 1996). On the other hand, a few SiO detections have been confirmed in regions VIII and V (mostly in region VIII).

Region VIII involves AGB stars, post-AGB stars, young stellar objects (dense cores in star-forming regions), and galaxies (van der Veen, Habing 1988; Stuers, Zealey 1991; Pashchenko, Le Skeren 1994). About 60% of the LRS spectra of bright IRAS sources in region VIII show weak-to-moderate 10 μ m absorption. Then, about 30% of the LRS spectra are typical for planetary nebulae (van der Veen, Habing 1988). The associations of IRAS sources with previously known objects were also studied by van der Veen, Habing (1988); 3% of the IRAS sources in region VIII are associated with a planetary nebula and 4% with an early-type star with emission lines. A relatively large fraction (15%) is associated with galaxies. However, most IRAS galaxies exhibit 12 μ m flux densities of less than 2 Jy (Fullmer, Lonsdale 1989), which equals the lower limit of the 12 μ m flux density of the present sample. Therefore, the possibility of the galaxies in the sample is excluded. Because young stars (or dense cores in star-forming regions) concentrate in the region of color larger than $C_{12} \simeq 1.0$ in the two color diagram (Stuers, Zealey 1991; Pashchenko, Le Skeren 1994), a majority of the objects in the sample would be late-type stars (AGB or post-AGB stars).

In the present sample, it would be appropriate that SiO-detected sources are classified as late-type stars (AGB or possibly post-AGB stars). SiO masers in star-forming regions are quite rare (Barvainis, Clemens 1984; Jewell et al. 1984). In fact, more than 99% of the SiO maser emitters previously known originate from late-type stars, except 3 extreme objects in star-forming regions: Orion IRc 2, W 51 IRs 2, and Sgr B2 MD5 (Hasegawa et al. 1986; Fuente et al. 1989; Morita et al. 1992). These objects in star-forming regions with SiO masers are surrounded by largely extended mid-infrared nebulosity. To check the contamination of young stellar objects in SiO detections, we inspected mid-infrared images toward SiO detections using MSX image archives with about 0.3' resolution (Price et al. 1997), but no extended source has been found toward SiO detections. In addition to the MSX images, we inspected nearinfrared J, H, K-bands images toward observed sources using the 2MASS image archive. The results of the inspection are given in table 1. Most objects with SiO masers were point-like. Some SiO detections were too faint to be seen in 2MASS near-infrared images. We found two objects with a large extended nebulosity: IRAS 19312+1950 and 20249+3953. Although the morphology of IRAS 20249+3953 in the 2MASS images was point symmetric (typically seen in post-AGB stars), we finally concluded that this object is a dense core in a star-forming region. An extended source and a dark lane were seen toward IRAS 20249+3953 in MSX and DSS images, respectively. About 10% of the present sample was recognized as star-forming regions using 2MASS images, and were non-detections in SiO masers.

The color index, C_{12} , which is believed to be an indicator of the evolutionary stage of

AGB stars, increases with the mass-loss rate. Near the end of the AGB phase, the mass-loss rate often increases enormously (up to $10^{-4}~M_{\odot}~\rm y^{-1}$; Blöcker 1995; Yamamura et al. 1996). The expansion velocity also increases ($\sim 20~\rm km~s^{-1}$); it is called superwind (Renzini 1981). The termination of a superwind is considered to be the end of the AGB phase (Renzini 1981). The boundary between the AGB and post-AGB phases is considered to be roughly at $C_{12} \sim 0.5$ in the two-color diagram (e.g., Figure 3 in Nyman et al. 1998; van Hoof et al. 1997). After the mass-loss (and pulsation) ceases, circumstellar gases are not supplied from the central star; SiO masers disappear first among the circumstellar masers (OH, $\rm H_2O$ and SiO) in the O-rich circumstellar envelope, because SiO masers are emitted within a few stellar radii from the central star. Therefore, when a star goes into the post-AGB phase, SiO masers would abruptly blow out to cease. In other words, if the IRAS color is an evolutionary indicator, a clear edge of the distribution of SiO emitters would be recognized in an IRAS two-color diagram, which corresponds with the boundary between AGB and the post-AGB phase. In fact, the edge of the SiO maser distribution can be seen around $C_{12} \sim 0.5$ in figure 6, though it is obscured by contamination of young stellar objects.

According to above perspective, SiO emitters with IRAS colors just beyond $C_{12} \sim 0.5$ can be regarded as stars at an early post-AGB phase (or at a possibly very late AGB phase) decreasing/ceasing mass-loss. We found three SiO emitters with the IRAS colors, $C_{12} > 0.5$, in the present sample: IRAS 18135-1456 (OH15.7+0.8), 18450-0148 (W 43A), and 19312+1950. Two of them (IRAS 18450-0148 and 19312+1950) were the first detections in SiO masers. An SiO maser toward IRAS 18135—1456 was previously detected by Nyman et al. (1993). We detected SiO masers toward IRAS 18498-0017, which is also considered to be a candidate for a post-AGB star because of its color, $C_{12} = 0.46$. We suggest that SiO masers of these stars (except IRAS 18498-0017) are still alive in the "dying AGB wind" during the massloss reduction process accompanying the departure from the AGB phase (e.g., Engels 2002). The IRAS variability indices for IRAS 18135–1456 and 18450–0148 are 0 and 19, respectively, indicating that these two are not at the mira-type pulsating phase (almost equal to AGB phase), but at the post-AGB phase. The H₂O maser of IRAS 18135-1456 has tended to gradually fade during last 10 years; after 1993, the H₂O maser was detected only once in 1997 (Engels 2002). The velocity width of the H_2O maser emission of IRAS 18450-0148 ($\sim 170 \text{ km s}^{-1}$, Likkel et al. 1992) exceeds that of the OH emission ($\sim 14 \text{ km s}^{-1}$, te Lintel Hekkert et al. 1989), indicating that the objects have recently become a post-AGB star (Gómez et al. 1994). In the cases of IRAS 18498-0017 and 19312+1950, the IRAS variability indices are 96 and 77, respectively. The index for IRAS 18498-0017 is somewhat too high to be regarded as a post-AGB star. Although H₂O and OH masers have been detected toward this object, the profiles of masers are like normal double peaks typically seen in AGB stars (te Lintel Hekkert et al. 1989; Engels et al. 1986). A relatively high value of the IRAS variability index of IRAS 19312+1950 might mean that this object is still at the AGB phase. However, Nakashima, Deguchi (2000)

reported that IRAS 19312+1950 has an extended near-infrared counterpart, which is typically seen in proto-planetary nebulae.

In order to check the contamination by interstellar dust in the IRAS 60 μ m flux densities, we made color–latitude diagrams, plots of IRAS colors, C_{12} and C_{23} , against the galactic latitudes, as shown in figure 7. In both panels in the figure 7, clear concentrations of the sources toward the galactic plane $(b=0^{\circ})$ can be seen. This concentration would be partly due to contamination by young stellar objects which are bound within $|b| \leq 1^{\circ}$. Another remarkable characteristic in figure 7 is a clear separation in the distribution between SiO detections and non-detections. IRAS colors of SiO detections do not strongly depend on the galactic latitudes except a few post-AGB candidates; this means that the IRAS colors well reflect the colors of the objects themselves in the case of SiO detections. In the upper panel of figure 7, the concentration of non-detections (open circles) around $C_{23} \sim 1$ is remarkable. Some of these sources are, in fact, known dense cores in star-forming regions. According to 2MASS near-infrared images, approximately 10% of the present sample is inferred to be young stellar objects in star-forming regions. Generally speaking, star-forming regions are recognized as a dense star cluster or an extended HII region in 2MASS images. In the present research, no SiO maser was detected toward young stellar objects.

The bulge SiO maser sources distribute quite differently in the color-latitude diagram; the color indices, C_{23} , of the SiO detections increase steeply up to ~ 0.5 near $|b| \sim 0^{\circ}$ (see figures 4 in Deguchi et al. 2000a, b). The SiO detections in the upper panel of figure 7 do not show such a behavior, except candidates for post-AGB stars with SiO masers (indicated by arrows in figure 7). Of course, post-AGB stars are supposed to have colors with higher C_{12} and C_{23} than do the other SiO detections. Therefore, we conclude that the IRAS colors, C_{23} of SiO detections in the present sample, are intrinsic to the sources, and that the contamination by interstellar dust in the IRAS 60 μ m flux densities in the present sample is relatively small. This is probably because the IRAS sources in the present sample are relatively bright objects $(F_{12} \geq 10 \text{ Jy})$ compared with those in the previous bulge samples (Deguchi et al. 2000a, b).

3.2. Intensity Ratio of the J = 1-0, v = 2 to v = 1 Lines

The intensity ratio of the SiO J=1-0, v=2 to the J=1-0, v=1 lines of AGB stars has been observed as being nearly equal to unity (Schwartz et al. 1979; Spencer et al. 1981; Nakada et al. 1993). Likewise, past results of SiO maser observations toward IRAS sources, which are normal AGB stars, have indicated that the intensity ratio was roughly unity (e.g., Izumiura et al. 1994). At a glance, it seems to be difficult to explain the intensity ratio of near unity of the two rotational lines in the different vibrational states with very different excitation temperatures as $T_{\rm ex}=1600$ K (v=1) and $T_{\rm ex}=3200$ K (v=2; e.g., Elitzur 1992). In order to explain it, Olofsson et al. (1981, 1985) proposed a line overlapping between the infrared transition of SiO (from v=1, J=0 to v=2, J=1) and a line of the H₂O molecule ($v_2=0$

 12_{75}) – (ν_2 =1 11_{66}), making a pump cycle between the SiO energy levels; J=0 $v=1 \Rightarrow J=1$ $v=2 \to J=0$ $v=2 \Rightarrow J=1$ $v=1 \to J=0$ v=1, where vibration–rotation and maser transitions are indicated by \Rightarrow and \rightarrow , respectively. This pump cycle, if it works, leads to a relative strengthening of the v=2 J=1–0 maser in comparison with the case of the absence of a pump cycle (Olofsson et al. 1985). On the other hand, however, there are many exceptional cases. For example, that the intensity ratio of IRC–10414 is less than about 0.1 (Imai et al. 1999). Nyman, Olofsson (1986) suggested that the average intensity ratio of SiO masers from OH/IR stars were nearly 4.

In the present research, we found a clue linking these intensity ratios of SiO masers. Figure 8 shows a plot of intensity ratios of the J=1-0, v=2 to the J=1-0, v=1 line (using the integrated and peak intensities) against the IRAS color index, C_{12} . The filled marks show the data in the present observation and the open marks indicate the data from a previous SiO maser survey of the inner-disk IRAS sources with $C_{12} < 0.2$ (Nakashima, Deguchi 2002). Both of the sources are located in almost the same galactic longitude range. The triangles and inverse triangles show the lower and upper limits, respectively. We can see that the v=2/1 line-intensity ratio tends to increase with the IRAS color of the objects until $C_{12}=0.5$. The average values of the intensity ratios of the open circles in figure 8 are nearly unity (the logarithmic values are nearly 0). In contrast, in cold IRAS sources with SiO masers (filled circles, $0.2 < C_{12} < 0.5$), the J=1-0 v=2 line, tends to be much stronger than the J=1-0 v=1 line as shown in figure 8. Beyond $C_{12} \sim 0.5$, the intensity ratios tend to decrease. The least-square best fits in the color range of $0.2 < C_{12} < 0.5$ (without upper and lower limits) in figure 8 give

$$\log(F_{v=2}/F_{v=1}) = 0.88 (\pm 0.13) C_{12} + 0.06 (\pm 0.03) \tag{1}$$

for the integrated intensity ratio, and

$$\log(T_{v=2}/T_{v=1}) = 0.56(\pm 0.07)C_{12} + 0.07(\pm 0.01) \tag{2}$$

for the peak-intensity ratio. Simple correlation coefficients are about 0.5 for both of the upper and lower panels in figure 8.

In the present observations, both SiO transitions, J = 1-0, v = 1 and 2, are near to the band edges of the SIS receiver with a band width of about 0.4 GHz. Therefore, the sensitivity at each frequency varies depending on the daily tuning condition of the receiver. Therefore, we carefully checked the reliability of the intensity calibration at different nearby frequencies using pointing sources and a molecular cloud, Sgr B2 every day, and confirmed that the intensity calibrations of all spectrometers were nearly equal through all of the observing sessions. Nyman et al. (1993) made a same plot with figure 8 using the (K-L) color as a horizontal axis, and found same correlation between the intensity ratio and the (K-L) color. The discrepancy of the correlation (in our case, seen at $C_{12} = 0.5$) could not be seen in Nyman et al.'s(1993) result.

Here, we would like to suggest an interesting resemblance with SiO masers in star-forming regions: Orion IRc 2, W 51 IRs 2, and Sgr B2 MD5 (Hasegawa et al. 1986; Fuente et al. 1989;

Morita et al. 1992). The line intensity ratios in the latter two SiO masers in star-forming regions greatly deviate from unity. The intensity of the J = 1-0, v = 1 line from Sgr B2 is about 1.5 Jy, while that of the J = 1-0, v = 2 line is less than 0.3 Jy (Shiki et al. 1997). In the case of W 51 IRs2, the J=1-0, v=2 intensity is more than 10-times stronger than that of J=1-0, v=1. Among these three objects, only Sgr B2 MD5 is included in the IRAS point source catalog (IRAS 17441-2822) and the IRAS colors are available $[(C_{12}, C_{23})=(0.95, 2.28)]$. These colors of Sgr B2 MD5 might suffer from serious contamination by surrounding material. According to mid-infrared photometry for the Ori KL region with SiO masers by Gezari et al. (1998), the mid-infrared color of IRc2 (a logarithmic ratio of the 12 to 20 μ m intensity) is about 0.2. For the case of W 51 IRs2, it is somewhat difficult to estimate the mid-infrared fluxes because this source consists of at least 7 continuum sources; four of them are ultra-compact HII regions 2001). For the moment, we estimate the color of W 51 IRc2 to be $C_{12} \sim$ (Okamoto et al. 0.6 by extrapolating the spectrum in figure 2 of Okamoto et al. (2001) to longer wavelengths. Therefore, the increasing color sequence of these three sources is "Orion IRc 2—W 51 IRs 2—Sgr B2 MD5". The observed line-intensity ratios to the mid-infrared color for these three sources are consistent with the correlation shown in figure 7. The ratio increases with C_{12} , but decrease beyond $C_{12} \sim 0.5$. Therefore, the line intensity-color correlation found in the evolved stellar objects also seems to be applied to the SiO maser sources in the star-forming regions, and may be useful to deduce the pumping mechanism of SiO masers.

3.3. Longitude Distribution

Figure 9 shows a histogram of the galactic longitudes for the SiO detections (shadow) and non-detections (blank). The detection rates are also shown by solid line with filled circles. For a comparison, the detection rates in the previous SiO maser surveys of sources with IRAS colors of typical AGB stars are also shown by the dotted line with filled squares (Izumiura et al. 1999; Deguchi et al. 2000aa; Deguchi et al. 2000a, b; Nakashima, Deguchi 2002; Nakashima et al. 2002). The detection rate in this sample tends to decrease with the galactic longitude, as found in previous SiO surveys of IRAS sources with the color $0.0 < C_{12} < 0.1$. We then see a sudden increase in the detection rate in the range between $l=20^{\circ}$ and 40° . Because we used the MSX positions instead of the IRAS positions in the inner region $(l < 40^{\circ})$, the difference in the survey condition can possibly be a cause of the sudden change of the detection rates; the detection rate is 55% for 53 sources in $l < 40^{\circ}$, and 24% for 90 sources in $l > 40^{\circ}$. However, the improvement of the positions is not enough to make the overall change in the detection rates above and below $l = 40^{\circ}$, because the number of MSX counterparts with a large separation (> 20'') from the IRAS position was only 3 in the present sample. The maximum of the detection rate between $l = 20^{\circ}$ and 40° may be caused by a statistical fluctuation due to the small numbers of observed sources in the bin.

Figure 10 shows a longitude-velocity diagram for SiO detections overlaid on the CO

J=1–0 line map (taken from Dame et al. 2001). The filled and open circles indicate the sources with distances (luminosity distance; see next paragraph) below and above 5 kpc. The spread of the radial velocities of the SiO sources seems to be within the velocity limits produced by galactic rotation, which is indicated by the CO gas distribution [except IRAS 17545–2512 at ($l=43^{\circ}56$, $V_{\rm lsr}=-126$ km s⁻¹, and $D_L=4.4$ kpc)]. The upper edge of the SiO distribution corresponds to the Sagittarius–Carina arm and the Scutum–Crux arm at a distance of 4–5 kpc, and the lower edge (between $l=30^{\circ}$ and 100°) corresponds to the outer arm at a distance of 8–10 kpc. We found that only one source in our sample, IRAS 17192–3206 at $l=-53^{\circ}4$, has a large negative velocity; this source is probably associated with the central nuclear disk which is rapidly rotating, as seen in the overlaid CO map.

Figure 11 shows the distribution of SiO detections projected onto the Galactic plane. The SiO sources in the present sample do not show any systematic patterns in figure 11. As in previous papers, the distances (luminosity distance) were estimated from the bolometric fluxes of sources which were computed from IRAS 12 and 25 μ m flux densities and a bolometric correction for O-rich stars (van der Veen and Breukers 1989) based on the assumption of a constant luminosity of $8 \times 10^3 L_{\odot}$. For post-AGB stars, the bolometric flux tends to be underestimated in the bolometric correction, because the spectral energy distributions of post-AGB stars are weighted at shorter and longer wavelengths, which is different from those of AGB stars. Because the AGB stars have a single-peak spectral energy distribution, which is peaked at a mid-infrared wavelength, the bolometric correction is relatively accurate. In contrast, post-AGB stars have a doubly peaked SED, peaked at the mid and near-infrared wavelengths (e.g., Fujii et al. 2002). To make more precise bolometric corrections for post-AGB stars, we need to obtain near-infrared fluxes.

We also calculated the radial velocity dispersion (root mean squares of residues subtracted by circular and solar motions from $V_{\rm lsr}$) for the 22 SiO sources in 40° < l < 70°, and obtained the dispersion 27.9 km s⁻¹. Here, a flat rotation curve (see caption of figure 7 in Nakashima, Deguchi 2002) and the galactocentric distance of the Sun (8.5 kpc) are assumed in the calculation. This value is comparable with the dispersion, ~30–35 km s⁻¹, for the SiO sources with the bluer IRAS colors (C_{12} < 0.2) in several galactocentric distance ranges (Nakashima, Deguchi 2002). This value is also comparable with the dispersion of ~30 km s⁻¹ for the nearby SiO maser sources in the southern hemisphere (Deguchi et al. 2001b). For the subsample of 29 sources in l < 40°, we obtained a slightly larger radial velocity dispersion, 35 km s⁻¹. This subsample might give a larger velocity dispersion caused by the errors involved in the distance estimations.

4. Individual Sources

Among the observed sources, the known young stellar objects in star-forming regions are IRAS 17271-3309 (Bronfman et al. 1996), 18196-1331 (Minchin et al. 1991; Kastner et

al. 1992; Geballe, Oka 1996), 18551—0146 (Watt & Mundy 1999), 19089+1542 (Thé et al. 1994; Meeus et al. 2001), 19598+3324 (Cesaroni et al. 1988), 20187+4111 (Hillenbrand et al. 1995). Notable evolved stars are as follows;

These sources were studied as maser sources associated with a globular cluster, Liller 1. However, because of radial velocity differences (Sevenster et al. 1997; te Lintel Hekkert et al. 1991b; te Lintel Hekkert et al. 1989), Frail, Beasley (1994) concluded that these are not associated with Liller 1. SiO masers were detected in the present research, and radial velocities coincided with those of OH masers.

IRAS 18016-2743

The OH 1612 MHz maser was detected (te Lintel Hekkert et al. 1991b; David et al. 1993; Sevenster et al. 1997), but SiO maser searches have been negative in the J = 2-1 v = 1 line (Nyman et al. 1998) and in the J = 1-0 v = 1 and 2 lines in the present paper. This object was classified as a proto-planetary nebula by Nyman et al. (1998).

IRAS 18071-1727 (OH 12.8 +0.9)

The OH 1612 MHz maser was detected from this object (te Lintel Hekkert et al. 1989; David et al. 1993). SiO maser searches (J = 1–0 v = 1 and 2, and J = 2–1 v = 1) have been negative (Nyman et al. 1998; this paper). This source was not resolved ($\leq 1''$) in mid-infrared imaging observations (Meixner et al. 1999). Nyman et al. (1998) classified this source as a proto-planetary nebula.

IRAS 18450-0148 (W 43A)

The velocity width of H_2O maser emission of this source (~ 170 km s⁻¹, Likkel et al. 1992) exceeds that of the OH maser emission (~ 14 km s⁻¹, te Lintel Hekkert et al. 1989), indicating that this source recently entered the proto-planetary phase (e.g., Gómez et al. 1994). Imai et al. (2002) found a collimated and precessing jet of molecular gas that is traced by H_2O maser spots.

IRAS 19069+0916

Both the SiO and $\rm H_2O$ masers were detected in this research. SiO emission was found at $V_{\rm lsr} = 30.0~{\rm km^{-1}}$, though $\rm H_2O$ masers were detected at $V_{\rm lsr} = -25.7$ and $10.7~{\rm km^{-1}}$ in the present paper (figure 5). The OH 1612 MHz double peaks were found at $V_{\rm lsr} = 10$ and 54 km s⁻¹ (Eder et al. 1988), giving the stellar velocity at $V_{\rm lsr} \sim 32~{\rm km~s^{-1}}$; this is consistent with the SiO radial velocity. The low-velocity component at $V_{\rm lsr} = -26~{\rm km~s^{-1}}$ of $\rm H_2O$ maser emission, which appears lower than the velocity expected from the OH double peaks, had not been detected in the past (Engels, Lewis 1996). It might indicate an activity of the central star at a transient stage to the post-AGB phase.

IRAS 19312+1950

A large extended nebulosity can be recognized in 2MASS images toward this source. Nakashima, Deguchi (2000) found SiO and H_2O maser emissions. They also reported tentative detections of HCN and SO thermal lines toward this source.

IRAS 19327+3024 (BD+30°3639)

This is a planetary nebula, and has been rigorously observed from X-ray to radio wavelengths, including optical imaging with the HST (Harrington et al. 1997). The relatively low temperature of the central star ($T \sim 40000 \text{ K}$) and the small expansion time scale of the nebula (900 yr; Kawamura, Masson 1996) suggests a recent emergence to the planetary-nebula phase. No maser has ever been detected.

5. Conclusion

We observed 143 cold IRAS sources in the SiO J=1-0, v=1 and 2 lines, and detected 51 objects; 45 of 51 are new detections. SiO masers were newly detected in two candidates for post-AGB stars: IRAS 18450-0148 (W 43A) and 19312+1950. We also detected 3 H₂O maser emitters out of 23 observed sources; one of them was a new detection. The main results of this research are:

- 1. The intensity ratio of the SiO J=1-0, v=2 to the J=1-0, v=1 lines is correlated with the IRAS color for objects with $C_{12} \lesssim 0.5$. Beyond $C_{12} \sim 0.5$, the intensity ratio dramatically drops.
- 2. The IRAS colors, C_{12} and C_{23} , of SiO emitters near the Galactic plane do not strongly depend on the galactic latitude, though the colors of SiO non-detections tend to vary with the latitude. This fact indicates that young stellar objects contaminate the sample, and that the IRAS colors of SiO emitters reflect the intrinsic colors of the objects themselves.
- 3. The SiO sources are not strongly associated with the spiral arms in the longitude–velocity diagram and on the Galactic-plane map. The velocity dispersion of the SiO detections in the sub sample ($l > 40^{\circ}$) is comparable with the dispersions found in previous SiO surveys for sources with different colors (typical colors of normal AGB stars). These facts suggest that the cold IRAS sources with SiO masers has a kinematic property very similar to that of typical AGB stars with SiO masers.

The authors thank staff of Nobeyama radio observatory for the help of observations and also thank Y. Ita and T. Soma for the help in the data reductions. This research is made use of the SIMBAD database, operated at CDS, Strasburg, France and also made use of the 2MASS and MSX data archive, operated at IRSA, NASA. This paper is a part of the JN's thesis presented for the award of Ph. D. to the Graduate University for Advanced Studies.

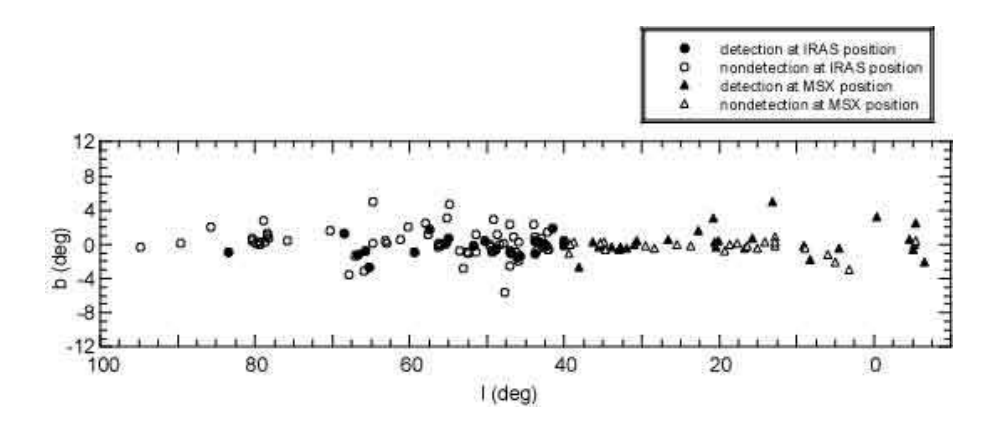


Fig. 1. Positions of the observed sources in the galactic coordinates. The circles and triangles indicate sources observed at IRAS and MSX positions, respectively. The filled and open marks indicate SiO detections and nondetections, respectively.

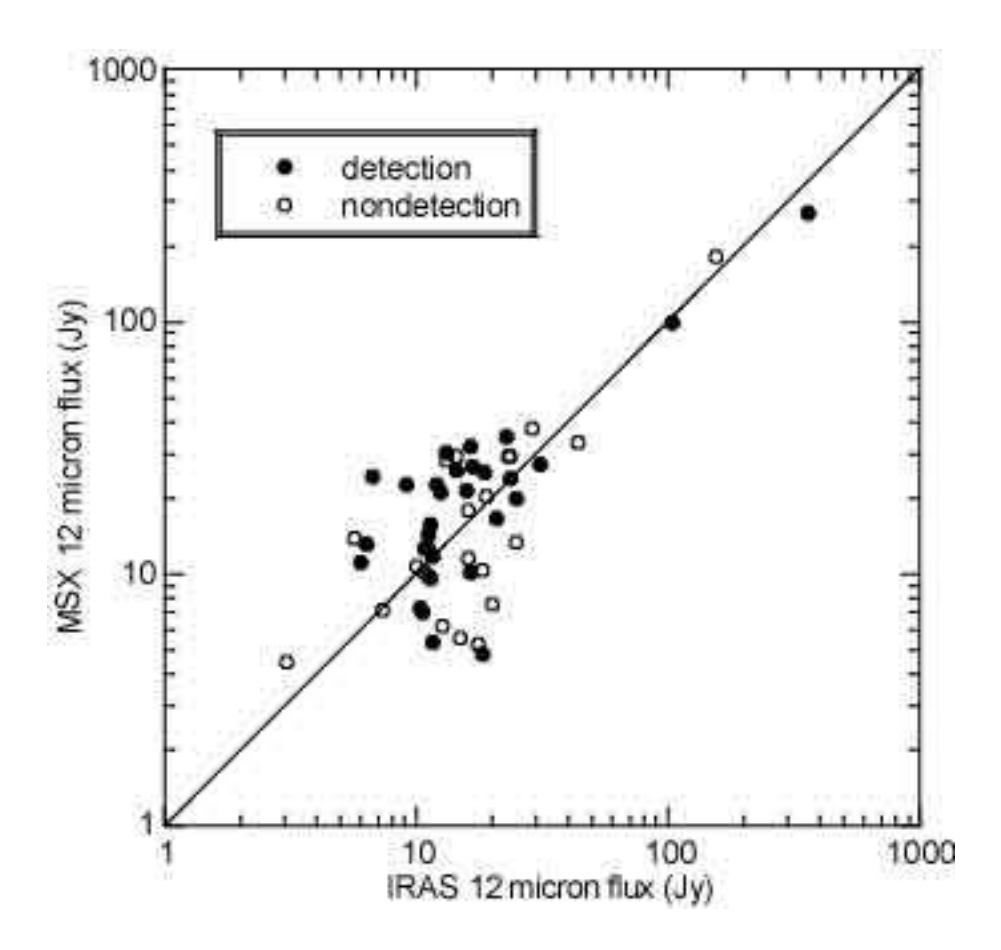


Fig. 2. Correlation between IRAS and MSX 12 μ m flux densities for the sources with $l < 40^{\circ}$.

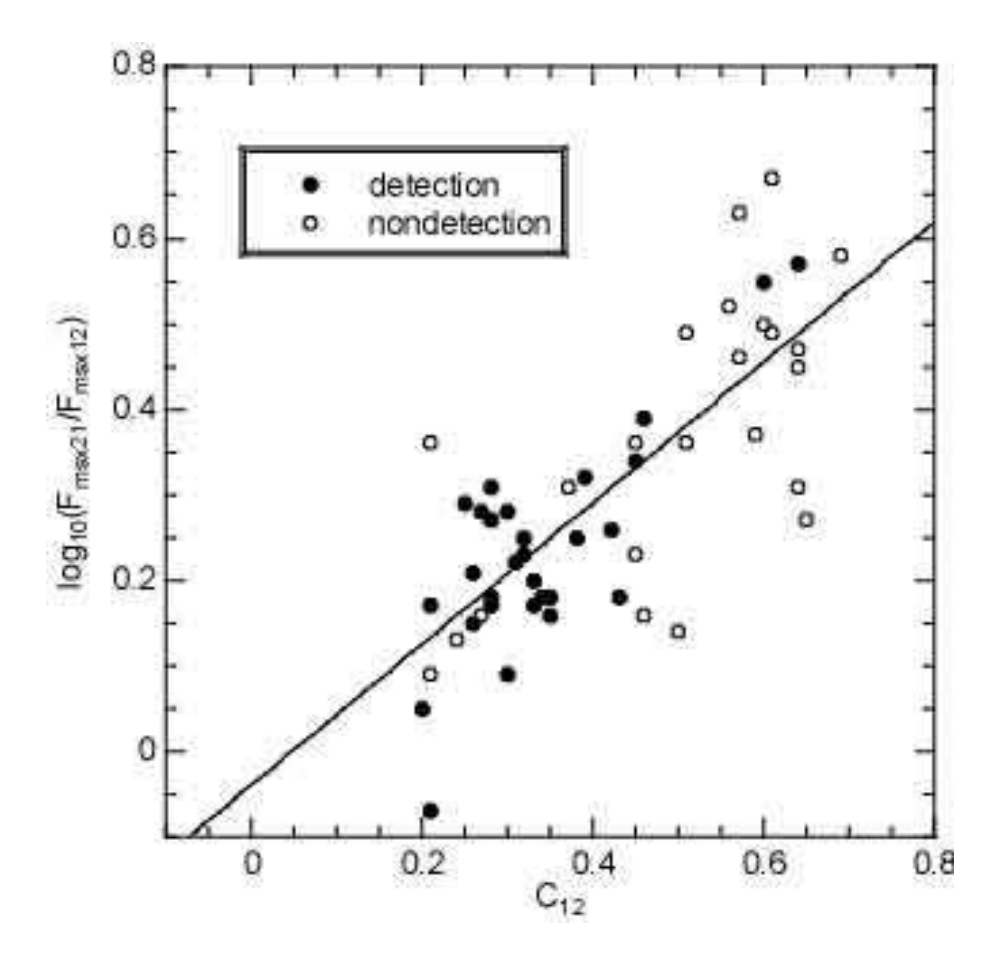


Fig. 3. Correlation between IRAS and MSX colors for the sources with $L < 40^{\circ}$. $F_{\rm msx12}$ and $F_{\rm msx21}$ indicate the MSX flux densities at 12 (C-band) and 21 (E-band) $\mu{\rm m}$.

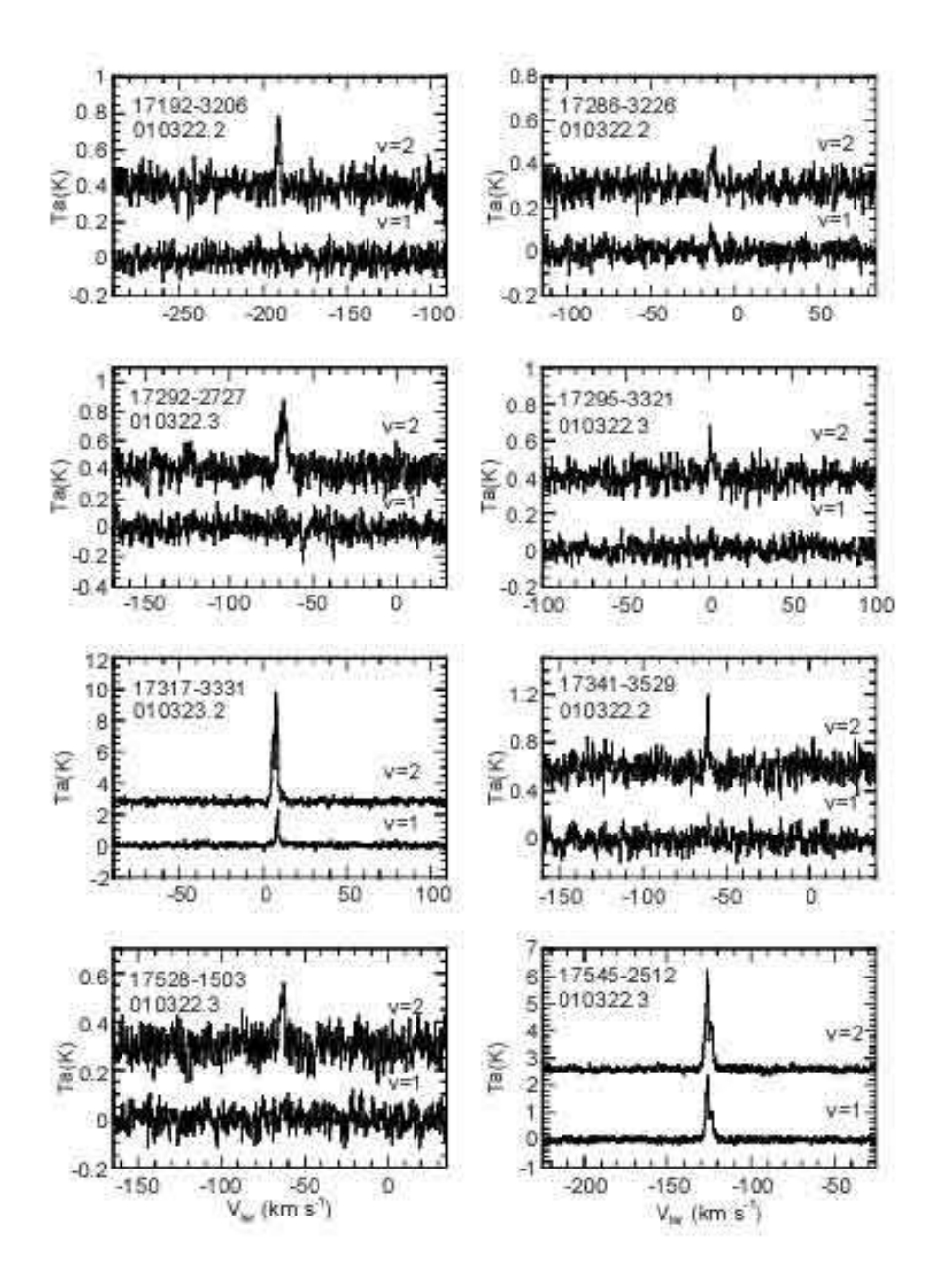


Fig. 4a. Spectra of the SiO J = 1-0, v = 1 and 2 lines for 50 of 51 detected sources, except for IRAS 19312+1950 (e.g., Nakashima, Deguchi 2000)

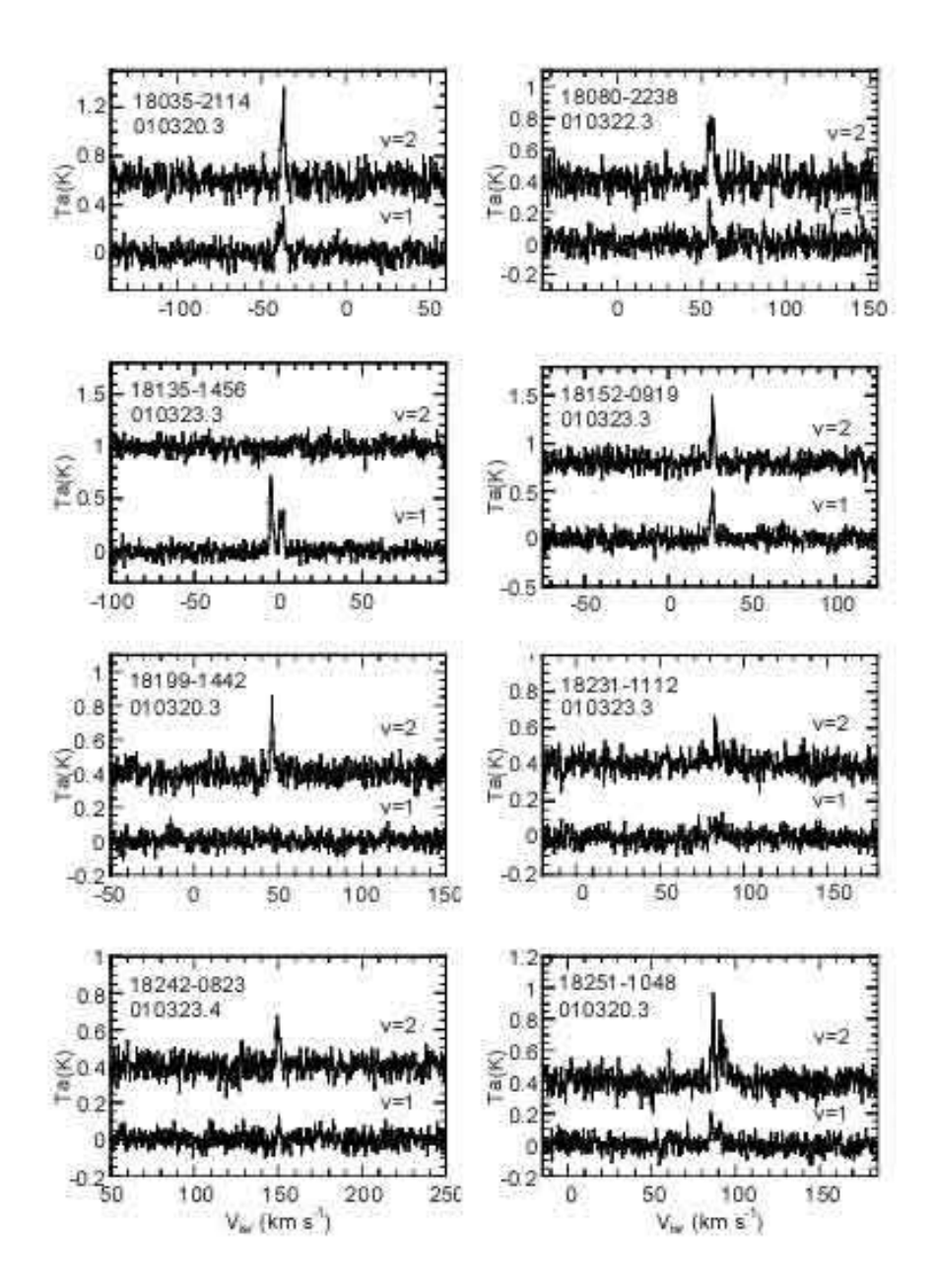


Fig. 4b. Continued.

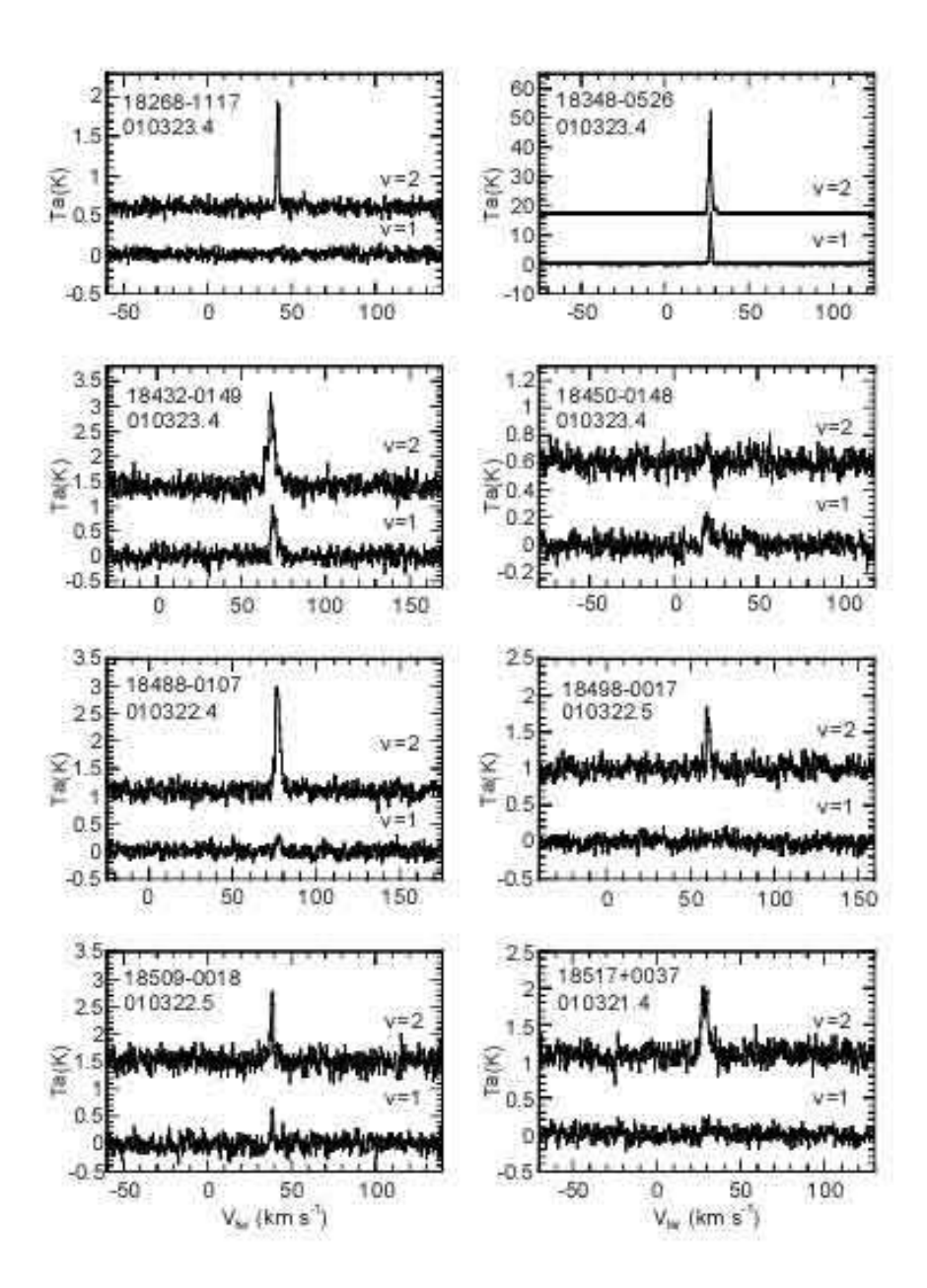


Fig. 4c. Continued.

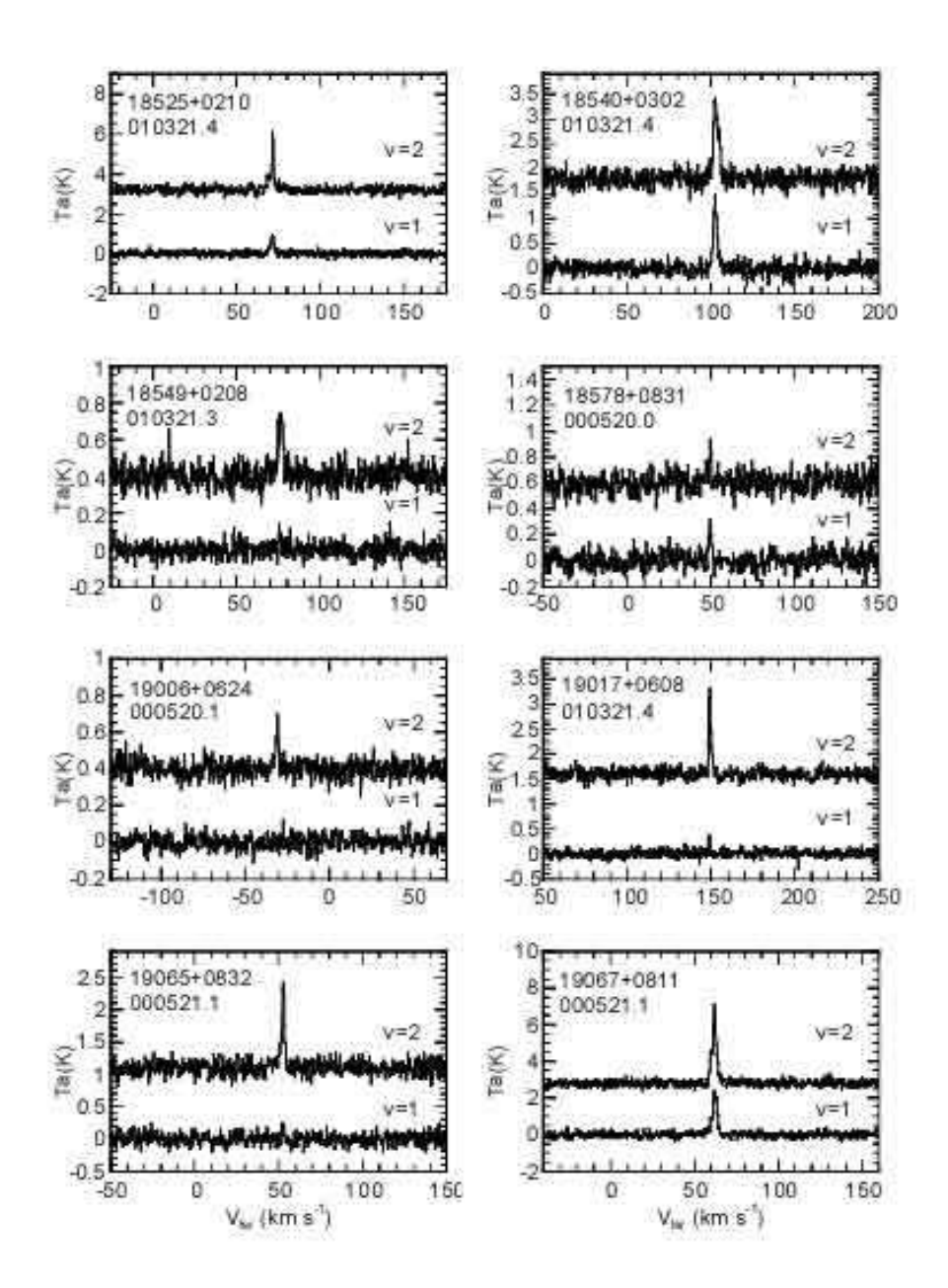


Fig. 4d. Continued.

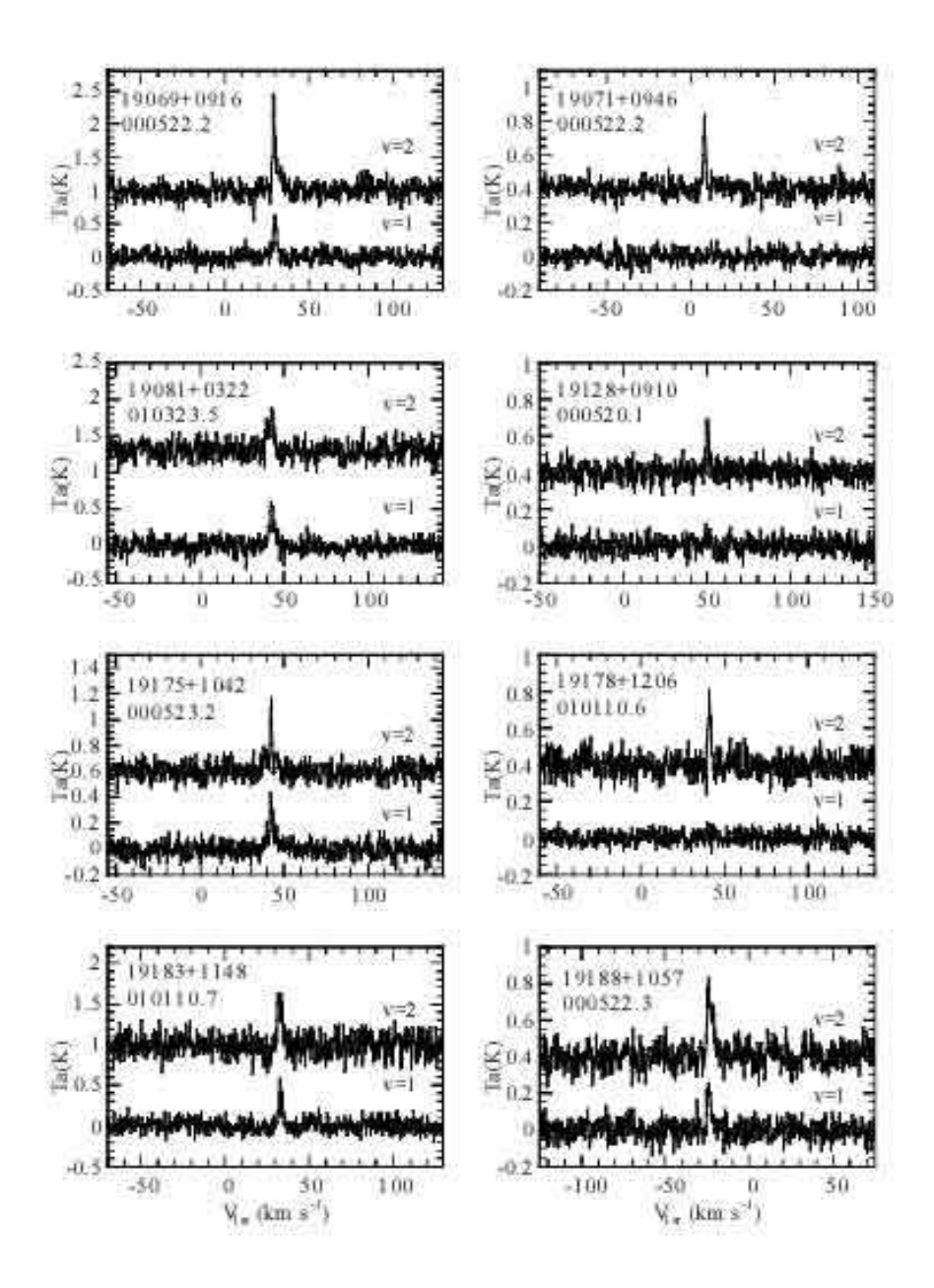


Fig. 4e. Continued.

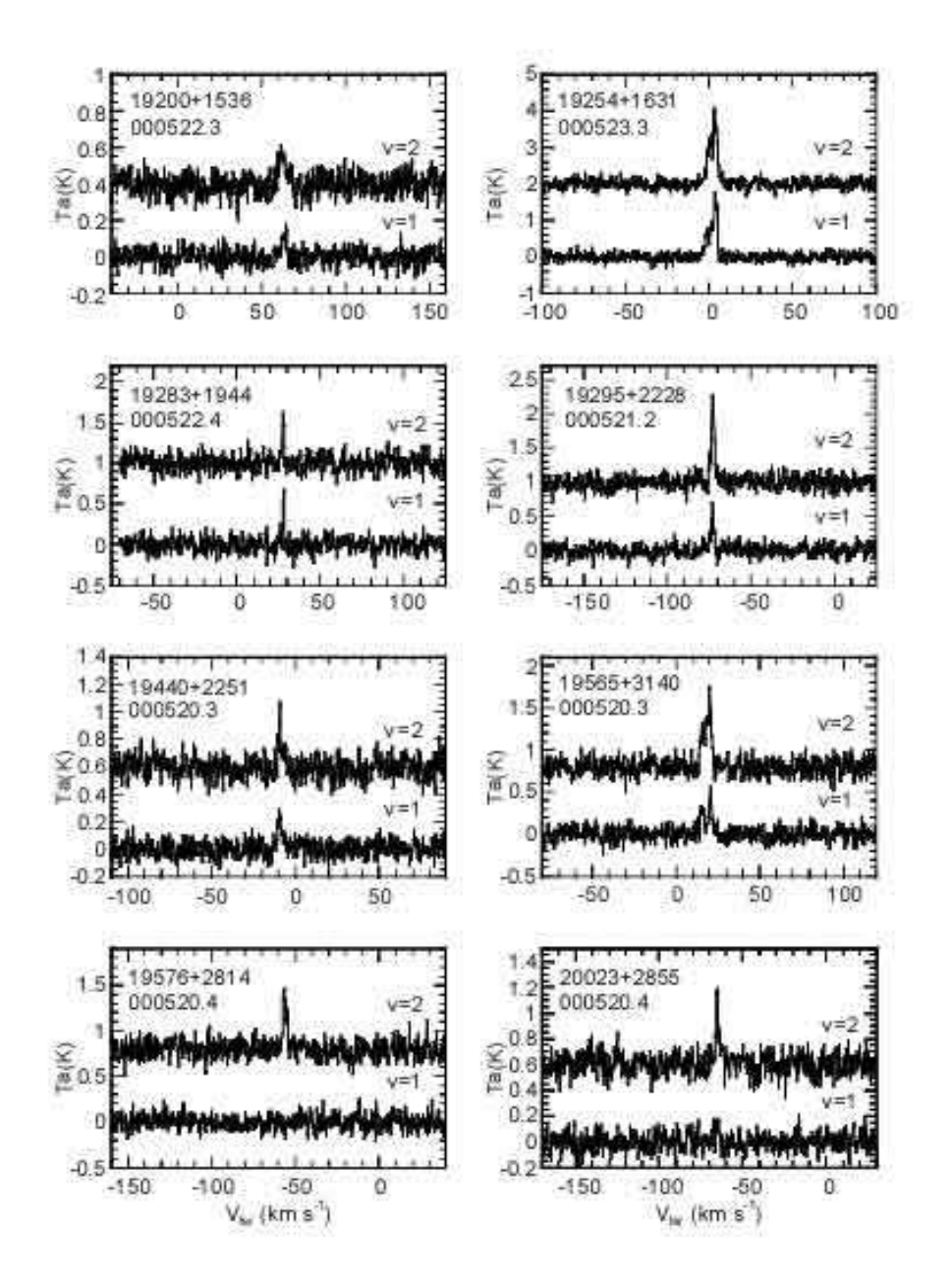


Fig. 4f. Continued.

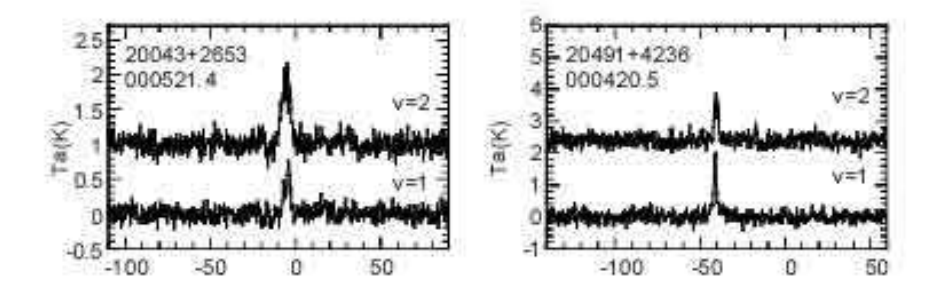


Fig. 4g. Continued.

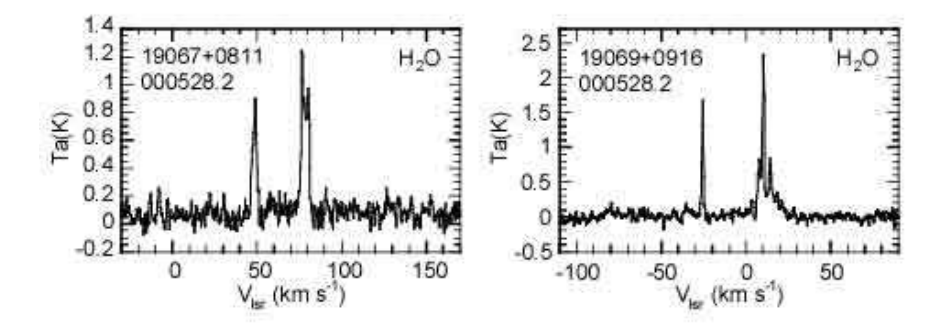


Fig. 5. Spectra of the H₂O maser line at 22 GHz for 2 of 3 detected sources except IRAS 19312+1950 (e.g., Nakashima, Deguchi 2000).

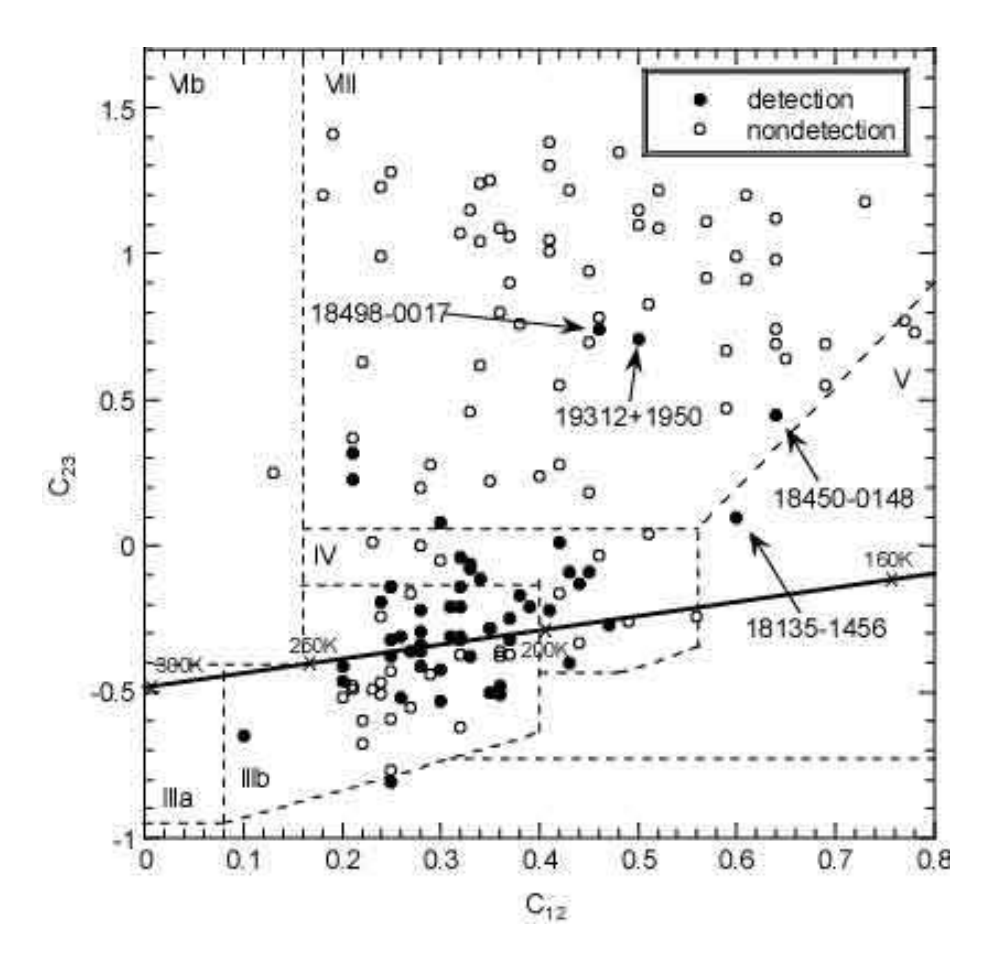


Fig. 6. IRAS two-color diagram of the present sample. The filled and open circles indicate SiO detections and non-detections, respectively. A black-body curve is indicated by a solid line. The fegions in the diagram indicate a classification of IRAS sources by van der Veen, Habing (1988). Candidates for post-AGB stars or late-AGB stars with extreme thick envelope are indicated by arrows.

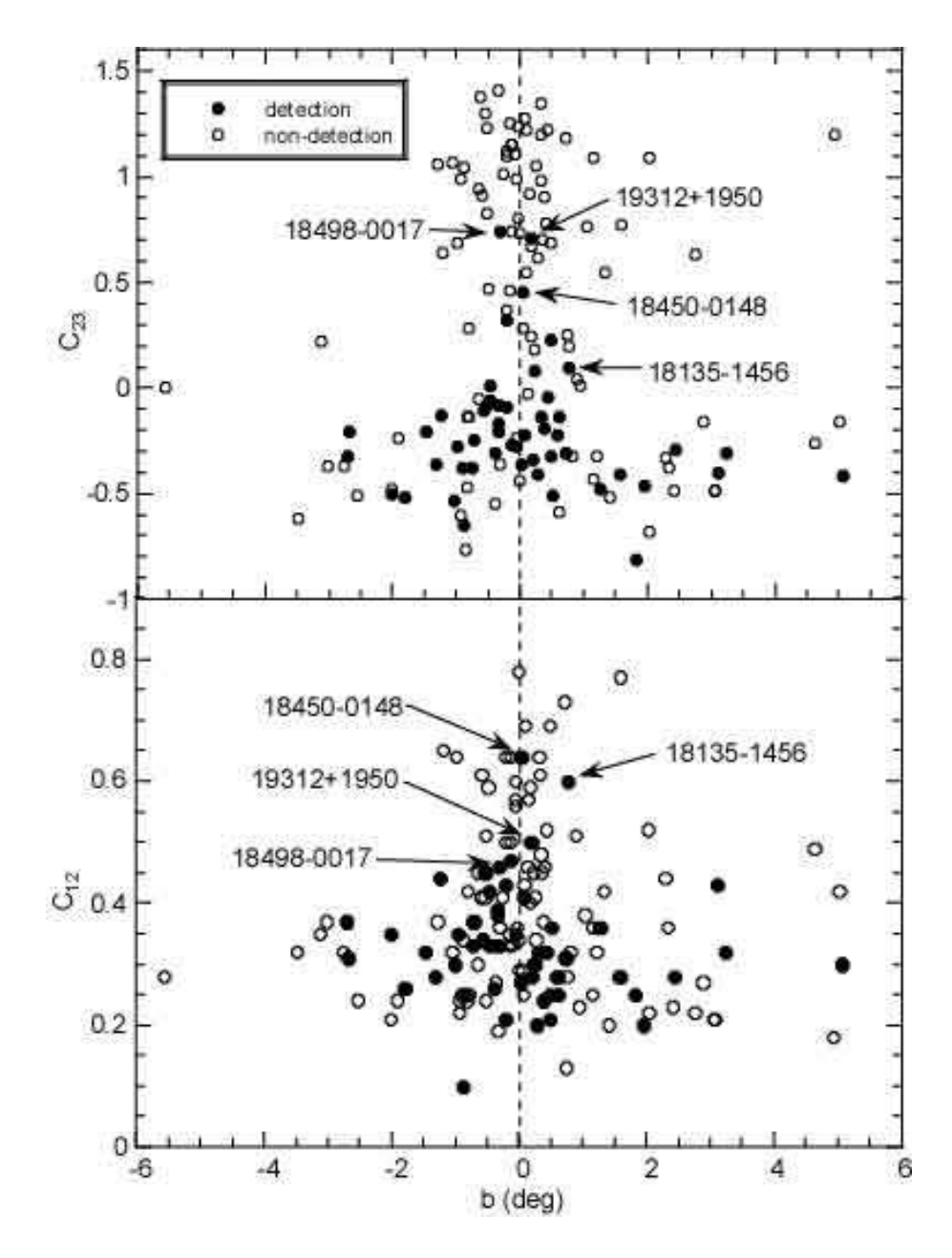


Fig. 7. Galactic latitude vs. IRAS colors. The filled and open circles are detections and non-detections in SiO, respectively. The names of the candidates for post-AGB stars (or late-AGB stars) with an extreme-thick envelope are indicated in the diagram.

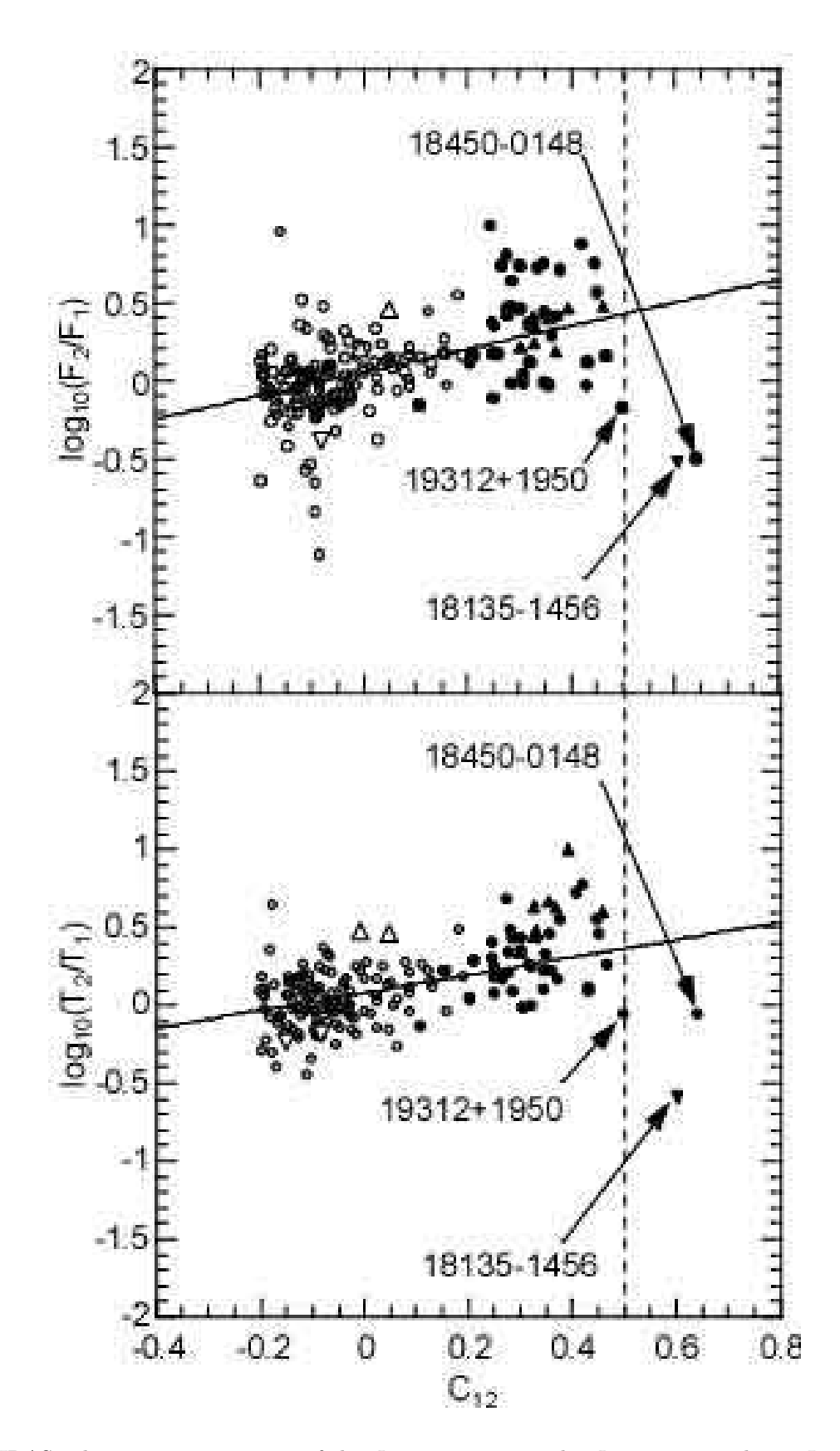


Fig. 8. IRAS color vs. intensity ratio of the J=1-0, v=2 to the J=1-0, v=1 lines. In the upper panel, the integrated intensities are used to calculate the intensity ratios. In the lower panel, the peak intensities are used. The filled and open marks indicate the present sample and the sample in previous SiO observations of normal AGB stars, respectively (Nakashima, Deguchi 2002). The triangles and inverse triangles represent the lower and upper limits, respectively. Candidates for post-AGB stars are indicated by arrows.

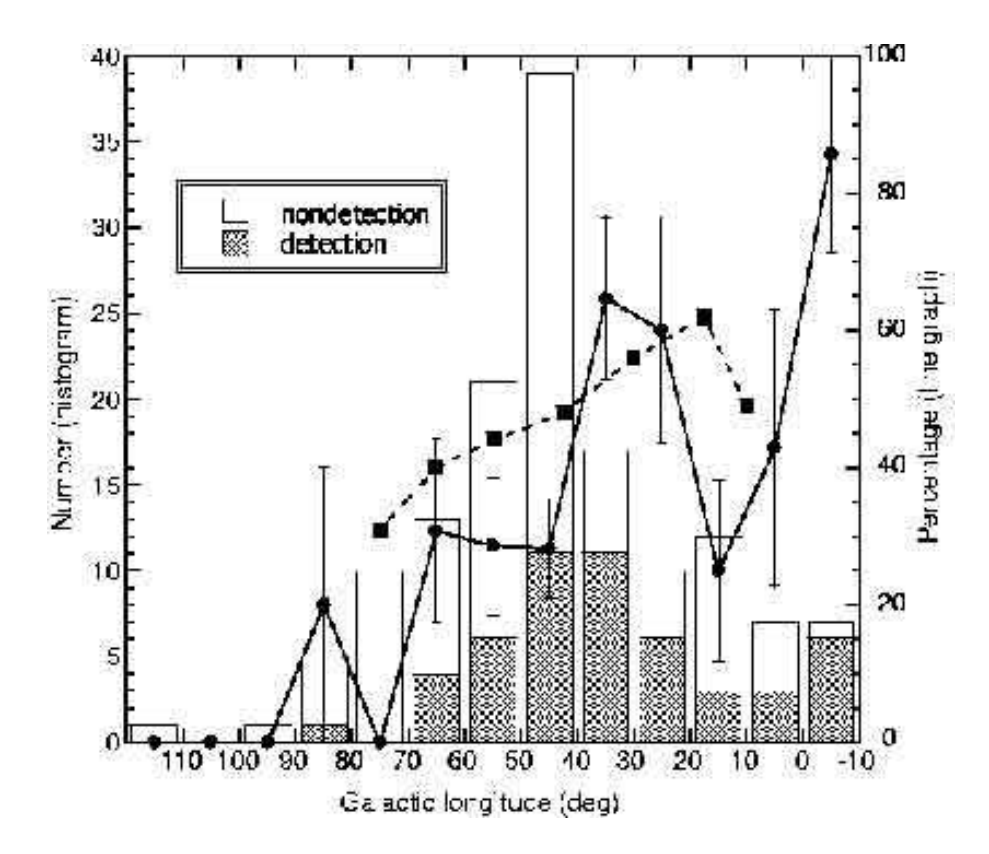


Fig. 9. Histogram of the present sample with the galactic longitude. The shaded and blank portions in the histogram indicate the number of SiO detections and non-detections, respectively. The line graph drawn by the solid line indicates the detection rate of the present SiO observations. The line graph drawn by the dotted line indicate the detection rate of an SiO observation for blue IRAS sources with the typical color of normal AGB stars (Nakashima, Deguchi 2002; Nakashima et al. 2002; Izumiura et al. 1999; Deguchi et al. 2000a, b). The error bars indicate the 95% confidence intervals.

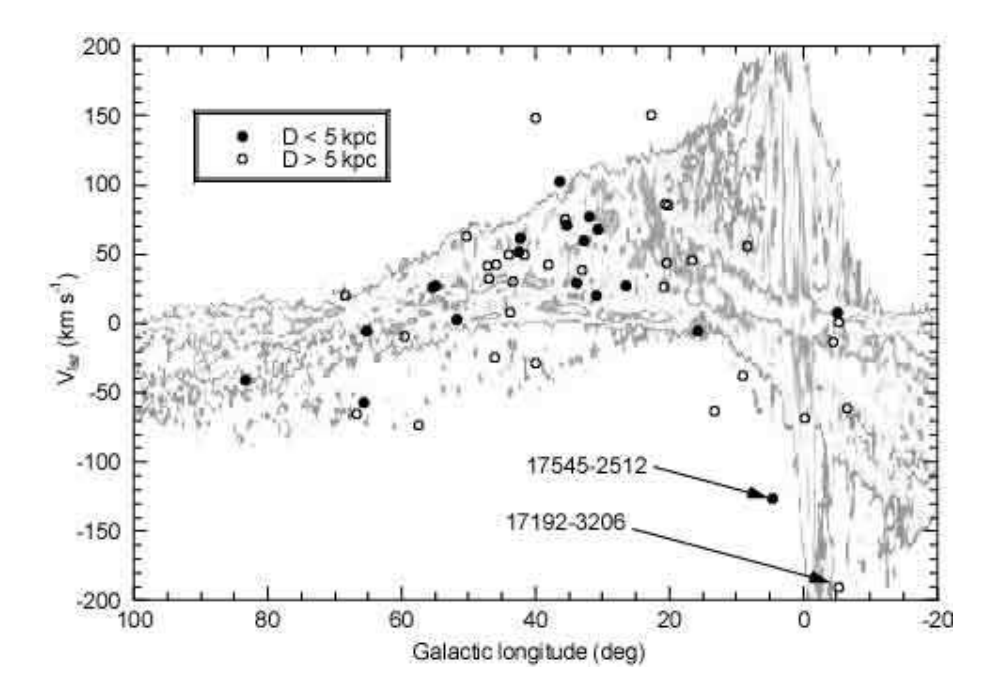


Fig. 10. Longitude-velocity diagram of the SiO detections overlaid on the CO v-l map (taken from Dame et al. 2001). The filled and open circles indicate sources at the distance above and below D=5 kpc, respectively. The distances used in here are luminosity distance, which is explained in the text. The sources with remarkable velocity are indicated by arrows.

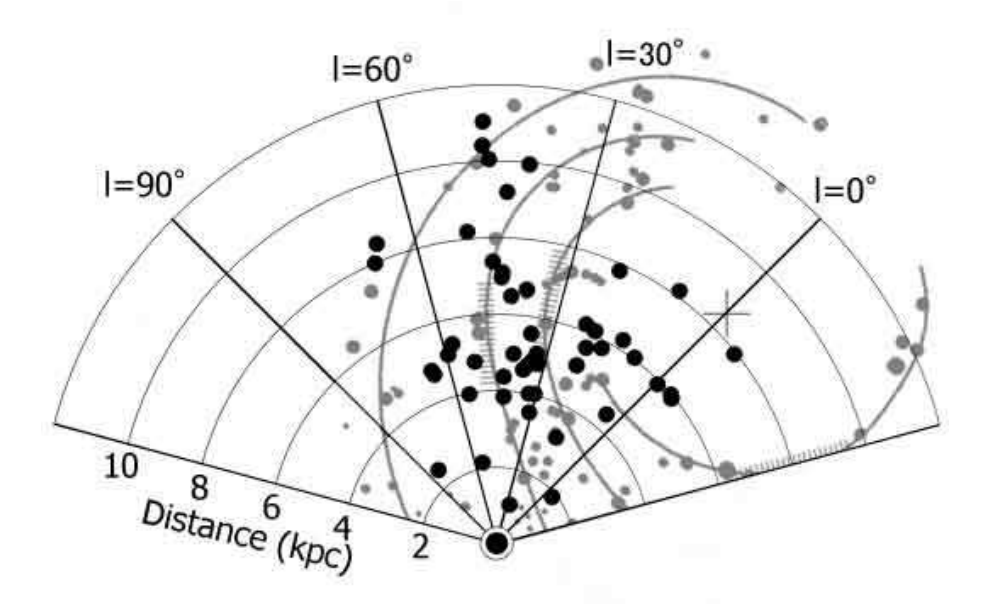


Fig. 11. Distribution of SiO detected sources projected onto the Galactic plane, overlaid on the spiral arm model of the Galaxy. The filled circles represent SiO sources. The large and small gray circles indicate HII regions, and the hatched areas correspond to the directions of the intensity maxima in the thermal radio continuum and neutral hydrogen emission (Taylor, Cordes 1993).

Table 1. IRAS Data.

$ \begin{array}{c ccccccccccccccccccccccccccccccccccc$	IRAS name	1	1.	E	<u> </u>	<i>C</i>	D	V (C:O)	MCV	C	01/1/00*
Try Try	IRAS name	l	b	F_{12}	C_{12}	C_{23}			MSX name	Sep.	ZMASS
17271-3300 354.66	17100 2200	\ /	()		0.00	0.20	\ - /	\ /	254 5070 + 00 4260	()	
17286-3226 355.44											-
17292-2727 359.66 3.23											
$\begin{array}{c} 17295-3321\ 354.76\ -0.06\ \ 11.300\ \ 0.35\ -0.28\ \ 6.0\ \ \ \ \ \ \ \ \ \ \ \ \ \ \ \ \ \ \ $											-
17317-3331 354.88 - 0.54											
17341-3529 353.50 - 2.02											-
17528-1503 13.14 5.06 10.310 0.30 - 0.42 6.3 -62.7 013.1444-16.6638 3 no 17545-2512 4.56 -0.40 20.730 0.26 - 0.31 4.4 -126.2 004.5628-00.3974 3 ps 18016-2743 3.18 -3.02 0.37 - 0.37 11.4 -0.03.1764-03.0243 2 ps 18016-2743 3.18 -3.02 0.37 - 0.37 11.4 -0.03.1764-03.0243 2 ps 18016-2540 4.97 - 2.02 13.00 0.21 - 0.48 5.5 -0.04.9722-02.0207 3 no 18035-2114 9.03 -0.21 0.32 8.2 -37.3 009.0299-00.2175 19 ps 18071-1727 12.76 0.90 23.660 0.51 0.04 3.8 -012.757+00.8951 4 no 18080-2238 8.33 1.10 1.10 0.26 - 0.52 6.1 55.5 088.3283-01.8028 9 ps 1812-1631 12.73 0.22 2.4960 0.64 1.12 3.4 .											-
$\begin{array}{c ccccccccccccccccccccccccccccccccccc$											-
18008-2419											
18016-2743 3.18 - 3.02 3.022 0.37 - 0.37 11.4 003.1764-03.0243 2 ps 18016-2540 4.97 - 2.02 13.100 0.21 - 0.48 5.5 004.9722-02.0207 3 no 18035-2114 9.03 - 0.21 5.957 0.21 0.32 8.2 -373.009.0299-00.2175 19 ps 18042-2131 8.87 - 0.49 11.230 0.59 0.47 5.3 008.8729-00.4928 10 ps 18071-1727 12.76 0.90 23.660 0.51 0.04 3.8 012.7577+00.8951 4 no 18071-1727 12.76 0.90 23.660 0.51 0.04 3.8 012.7577+00.8951 4 no 18092-1742 12.77 0.33 15.050 0.61 1.20 4.5 012.7747+00.3351 6 no 18112-1801 12.73 -0.22 24.960 0.64 1.12 3.4 012.7263-00.2210 18 sf 18125-1631 14.18 0.22 10.660 0.45 0.18 6.1 014.1831+00.2299 3 ps 18135-1456 15.70 0.77 31.020 0.60 0.10 3.2 -4.9 015.7002+00.7711 7 no 18152-0919 20.82 3.10 14.480 0.43 -0.40 5.1 26.3 020.8253+03.0969 19 ps 18171-1630 15.13 -0.53 20.080 0.51 0.83 4.2 015.1296-00.5266 1 ps 18184-1449 16.36 -0.21 18.420 0.50 1.10 4.4 016.3609-00.2073 4 sf 18199-1442 16.65 -0.48 12.050 0.33 -0.06 5.8 46.0 016.6452-00.4833 1 ps 1823-1243 18.66 -0.06 16.200 0.60 0.99 4.4 018.6545-00.0582 12 sf 18231-1112 20.09 0.49 10.590 0.21 0.23 6.1 85.0 020.0897+00.4860 7 ps 18262-1233 19.26 -0.82 14.350 0.24 -0.47 5.3 019.2580-00.8184 16 ps 18348-0526 26.54 0.62 359.800 0.25 -0.14 1.1 27.2 026.5439+0.0188 16 ps 18348-0526 26.54 0.62 359.800 0.25 -0.14 1.1 27.2 026.5439+0.0188 16 ps 18438-0403 29.56 -0.82 14.350 0.24 -0.47 5.3 019.2580-0.8184 16 ps 18438-0403 29.56 -0.82 14.350 0.24 -0.47 5.3 019.2580-0.0188 16 ps 18438-0404 30.94 0.04 23.730 0.64 0.74 4.3 019.2580-0.0188 16 ps 18438-0407 30.88											-
18016-2540 4.97 -2.02 13.100 0.21 -0.48 5.5 004.9722-02.0207 3 no											-
$\begin{array}{c ccccccccccccccccccccccccccccccccccc$											-
$\begin{array}{c ccccccccccccccccccccccccccccccccccc$											
18071-1727 12.76 0.90 23.660 0.51 0.04 3.8 012.7577+00.8951 4 no											-
18080-2238 8.33 -1.80 11.110 0.26 -0.52 6.1 55.5 508.3283-01.8028 9 ps 18092-1742 12.77 0.33 15.050 0.61 1.20 4.5 012.7747+00.3351 6 no 18112-1801 12.73 -0.22 24.960 0.64 1.12 3.4 012.7263-00.2210 18 sf 18125-1631 14.18 0.22 10.060 0.45 0.18 6.1 014.1831+00.2209 3 ps 18135-1456 15.70 0.77 31.020 0.60 0.10 3.2 -4.9 015.7002+00.7711 7 no 18152-0919 20.82 3.10 14.480 0.43 -0.40 5.1 26.3 20.8253+03.0969 19 ps 18171-1603 15.13 -0.53 20.080 0.51 0.83 4.2 015.1296-00.5266 1 ps 18184-1449 16.36 -0.21 18.420 0.50 1.10 4.4 016.3609-00.2073 4 sf 18196-1331 17.64 0.15 154.800 0.57 0.92 1.4 017.6369+00.1568 14 ps 18199-1442 16.65 -0.48 12.050 0.33 -0.06 5.8 46.0 016.6452-00.4833 1 ps 18223-1243 18.66 -0.06 16.200 0.60 0.99 4.4 018.6545-00.0582 12 sf 18231-1112 20.09 0.49 10.590 0.21 0.23 6.1 85.0 20.0897+00.4860 7 ps 18242-0823 22.71 1.58 10.660 0.28 -0.41 6.2 150.0 022.7076+01.5775 10 ps 18262-1233 19.26 -0.82 14.350 0.24 -0.47 5.3 019.2580-00.8184 16 ps 18348-0526 26.54 0.62 359.800 0.25 -0.14 1.1 27.2 26.5439+00.1678 3 ps 18348-0438 25.55 -0.05 18.920 0.25 -0.14 1.1 27.2 26.5439+00.6178 3 ps 18418-0415 28.40 -0.38 28.970 0.27 -0.55 3.8 028.4037-00.3341 5 ps 18438-0107 31.98 -0.48 16.450 0.42 0.01 4.8 76.9 031.9853-00.3356 4 ps 18498-0017 32.83 -0.32 22.850 0.46 0.74 4.0 68.2 030.7152+00.4268 5 no 18438-0017 31.98 -0.48 16.450 0.42 0.01 4.8 76.9 031.9853-00.3356 4 ps 18498-0017 32.83 -0.32 22.850 0.46 0.74 4.0 60.1 032.8286-00.3155 5 ps 18509-0018 30.94 0.04 23.730 0.64 0.45 3.5 20.1 030.9444+00.0347 8 ps 1849											-
18092-1742 12.77 0.33 15.050 0.61 1.20 4.5											
$\begin{array}{c ccccccccccccccccccccccccccccccccccc$											-
$\begin{array}{c ccccccccccccccccccccccccccccccccccc$											
18135-1456 15.70 0.77 31.020 0.60 0.10 3.2 -4.9 015.7002+00.7711 7 no 18152-0919 20.82 3.10 14.480 0.43 -0.40 5.1 26.3 020.8253+03.0969 19 ps 18171-1603 15.13 -0.53 20.080 0.51 0.83 4.2 015.1296-00.5266 1 ps 18184-1449 16.36 -0.21 18.420 0.50 1.10 4.4											
$\begin{array}{c ccccccccccccccccccccccccccccccccccc$											-
18171-1603 15.13 -0.53 20.080 0.51 0.83 4.2											
$\begin{array}{c ccccccccccccccccccccccccccccccccccc$											-
$\begin{array}{c ccccccccccccccccccccccccccccccccccc$											-
18199-1442 16.65 - 0.48 12.050 0.33 - 0.06 5.8 46.0 016.6452 - 00.4833 1 ps 18223-1243 18.66 - 0.06 16.200 0.60 0.99 4.4 018.6545 - 00.0582 12 sf 18231-1112 20.09 0.49 10.590 0.21 0.23 6.1 85.0 020.0897 + 00.4860 7 ps 18242-0823 22.71 1.58 10.660 0.28 - 0.41 6.2 150.0 022.7076 + 01.5775 10 ps 18251-1048 20.67 0.24 6.668 0.30 0.08 7.8 861.0 020.6720 + 00.2398 3 ps 18262-1233 19.26 - 0.82 14.350 0.24 - 0.47 5.3 019.2580 - 00.8184 16 ps 18268-1117 20.43 - 0.34 12.370 0.39 - 0.21 5.6 43.4 020.4323 - 00.3441 5 ps 18348-0526 26.54 0.62 359.800 0.25 - 0.14 1.1 27.2 026.5439 + 00.6178 3 ps 18432-0149 30.72 0.43											
$\begin{array}{c ccccccccccccccccccccccccccccccccccc$											
$\begin{array}{c ccccccccccccccccccccccccccccccccccc$											
$\begin{array}{c ccccccccccccccccccccccccccccccccccc$											
$\begin{array}{cccccccccccccccccccccccccccccccccccc$											
$\begin{array}{cccccccccccccccccccccccccccccccccccc$											
$\begin{array}{cccccccccccccccccccccccccccccccccccc$											
$\begin{array}{cccccccccccccccccccccccccccccccccccc$											
$\begin{array}{cccccccccccccccccccccccccccccccccccc$											
$\begin{array}{cccccccccccccccccccccccccccccccccccc$											
$\begin{array}{cccccccccccccccccccccccccccccccccccc$											
$\begin{array}{cccccccccccccccccccccccccccccccccccc$										18	
$\begin{array}{cccccccccccccccccccccccccccccccccccc$	18432-0149									5	-
$\begin{array}{cccccccccccccccccccccccccccccccccccc$											
$\begin{array}{cccccccccccccccccccccccccccccccccccc$	18450-0148	30.94									
$\begin{array}{cccccccccccccccccccccccccccccccccccc$	18488 - 0107							76.9	031.9853-00.4854		
$\begin{array}{cccccccccccccccccccccccccccccccccccc$											
$\begin{array}{cccccccccccccccccccccccccccccccccccc$											
$\begin{array}{cccccccccccccccccccccccccccccccccccc$											
$\begin{array}{cccccccccccccccccccccccccccccccccccc$											
$\begin{array}{cccccccccccccccccccccccccccccccccccc$										6	
$\begin{array}{cccccccccccccccccccccccccccccccccccc$											
$\begin{array}{cccccccccccccccccccccccccccccccccccc$											
18549+0208 35.58 -0.33 13.070 0.33 -0.08 5.6 75.2 035.5811-00.3335 17 no											
1000											
											ps

Table 1. (Continued)

IRAS name	l	b	F	C_{12}	<u> </u>	D	V (S;O)	MSX name	Con	2MASS*
INAS hame	(°)	(°)	F_{12} (Jy)	C_{12}	C_{23}	(kpc)	$V_{\rm lsr}$ (SiO) (km s ⁻¹)	MSA Hame	(")	ZWIASS
18587+0521	38.87	0.32	$\frac{(3y)}{5.432}$	0.64	0.98	7.4	\ /	038.8744+00.3090	24	no
19006 + 0624	40.02	0.32	4.082		-0.19	9.9	-28.9			
19008+0530	39.25	-0.07	12.740	0.24 0.57	1.11	5.0		039.2483-00.0649	28	
19000+0950 $19011+0852$	42.27	1.41	6.284		-0.52	7.9				
19011+1049	44.00	2.30	9.395		-0.32	6.3		•••		F ~
19017+0608	39.91	0.02	16.500		-0.36	5.0		039.9158+00.0180	8	110
19017 + 0008 $19025 + 0613$	40.07		3.044	0.21	-0.30 1.15	11.5				1
19025+0013	40.07		3.044	0.33	0.46	11.5		•••		F ~
19020 + 0014 $19045 + 0518$		-0.13 -0.99	7.395	0.64	0.40	6.3			5	r ~
19049 + 0914 $19048 + 0914$	43.02	0.76	3.064	0.04	0.09	11.5				
19048 + 0914 $19057 + 1002$	43.84	0.70	3.973	0.23	0.20	10.1		•••		F ~
19057 + 1002 $19065 + 0832$	42.60	0.94 0.07	20.220		-0.22	4.4	52.2	•••		110
19005+0832 $19067+0811$		-0.07	24.630		-0.22 -0.27	3.8	62.0	•••		Po
19067 + 0811 $19069 + 0916$	43.28	0.32	4.798		-0.27 -0.14	9.2	30.1			Po
	45.28	$\frac{0.52}{2.33}$			-0.14 -0.38	7.6	30.1	•••	• • •	Po
19069+1335	43.76		6.851				8.3	•••	• • •	Po
19071 + 0946 $19077 + 0839$		$0.51 \\ -0.14$	7.943	0.50	-0.51	7.1 6.2	8.3	•••	• • •	r ~
	42.83		9.125		1.15			•••	• • •	
19080+0748			14.140	0.41	1.38	5.2	40.0	038.1932-02.6822		01
19081+0322		-2.68	9.089		-0.21	6.7			3	1
19085+0755		-0.65	4.630		-0.05	9.4	• • • •	•••	• • •	1
19089+1542	49.21	2.89	23.440		-0.16	4.2	• • • •	•••	• • •	F ~
19108+0901		-0.65	3.689	0.45	0.94	10.0	• • • •	•••	• • •	Po
19112+1220	46.50	0.81	3.697		-0.32	10.5	• • • •	•••		110
19123+1139	46.01	0.27	9.285	0.34	0.62	6.6	40.7	•••	• • •	110
19128+0910		-1.02	8.410		-0.53	7.0	49.7	•••	• • •	Po
19134+2131	54.87	4.64	5.058		-0.26	8.4	• • •	•••	• • •	Po
19143+1427	48.72	1.15	3.031	0.36	1.09	11.5	• • • •	•••	• • •	110
19167+1313	47.90	0.06	4.183	0.29	0.28	9.9	• • • •	•••	• • •	110
19171+1119		-0.94	14.190		-0.60	5.3		•••	• • •	Po
19175+1042		-1.32	7.519		-0.36	7.4	42.3	•••	• • • •	Po
19177+1333	48.32		4.814		-0.44	9.2		•••	• • • •	Po
19178+1206		-0.72	3.659		-0.25	10.4	41.3	• • •	• • • •	Po
19183+1148		-0.97	3.290		-0.28	11.0	32.7	•••	• • • •	Po
19188+1057		-1.47	4.020		-0.21	10.0	-24.0	•••	• • • •	ps
19195 + 1650		1.16			-0.43		• • • •	• • •	• • • •	no
19199 + 2100	55.13	3.07	19.040		-0.49	4.6	• • • •	• • •	• • •	no
19200 + 2101	55.14	3.05	30.900		-0.49	3.6	• • • •	• • •	• • •	no
19200 + 1536	50.37	0.48	6.059		-0.32	8.2	63.0	• • •	• • •	ps
19200 + 1035	45.96		3.409		-0.24	10.9	• • • •	• • •		r ~
19205 + 1447		-0.02	5.760	0.34	1.24	8.4	• • •	• • •	• • •	sf ?
19207 + 1348		-0.52	7.349	0.24	1.23	7.4	• • •	•••		P~
19207 + 1346		-0.54	4.172	0.41	1.30	9.6	• • • •	• • •	• • •	sf ?
19211 + 1432		-0.27	4.414	0.41	1.01	9.3		•••		sf?
19223 + 1359		-0.79	6.401		-0.14	8.0	• • •	•••		no
19226 + 1401		-0.82	6.401		-0.14	8.0		•••		ps
19228 + 1403		-0.86	6.401		-0.77	8.0		•••		ps
19244 + 1115			1346.000		-0.51	0.5		•••		ps
19254 + 1631		-0.22			-0.09	4.8	3.1	•••		ps
19270 + 1550		-0.89	6.048	0.34		8.2		•••		ps
19281 + 2308	57.91	2.42	4.612	0.23	-0.49	9.3		•••		ps

Table 1. (Continued)

IRAS name	l	b	F_{12}	C_{12}	C_{23}	D_{I}	$V_{\rm lsr}$ (SiO)	MSX name	Sep.	2MASS*
	(°)	(°)	(Jy)	- 12	- 20	(kpc)	$({\rm km \ s^{-1}})$		(")	
19283+1944	54.95	0.73	88.500	0.31	-0.31	2.1	27.8			ps
19294 + 1649	52.54	-0.93	6.694	0.24	0.99	7.8				ppn?
19295 + 2228	57.49	1.82	14.250	0.25	-0.81	5.3	-73.0			ps
19295 + 1637	52.37	-1.05	5.051	0.32	1.07	9.0				no
19310 + 1745	53.54	-0.80	12.300	0.42	0.28	5.6				ps
19312 + 1950	55.37	0.19	22.470	0.50	0.71	4.0	26.1			ppn?
19319 + 2214	57.55	1.22	3.182	0.32	-0.32	11.3				ps
19327 + 3024	64.78	5.02	89.390		-0.16	2.1		• • •		ps
19332 + 2028	56.15	0.08	6.116	0.25	1.28	8.1	• • •	• • •		ps
19340 + 2016	56.08	-0.17	3.374	0.35	1.25	10.9	• • •	• • •	• • •	no
19341 + 2038	56.41	-0.03	5.569	0.36	0.80	8.5	• • •	• • •		ps
19344 + 2457	60.20	2.04	4.946		-0.68	9.0	• • •	• • •		ps
19352 + 2030	56.41	-0.31	42.890		-0.36	3.0	• • •	• • •		ps
19365 + 1023		-5.57	3.066	0.28	0.00	11.5	• • •	• • •		ps
19374 + 1626		-2.76	4.067		-0.37	10.0	• • •	• • •		no
19421 + 2507	61.21	0.62	8.114		-0.59	7.1	• • •	• • •		no
19440 + 2251	59.48	-0.90	15.700		-0.38	5.1	-9.4	• • •		no
19473 + 2638	63.11	0.39	6.026	0.37	0.90	8.1	• • •	• • •		sf
19479 + 2620	62.92	0.09	4.574	0.43	1.22	9.1	• • •	• • •		no
19520 + 2759	64.81	0.18	46.850	0.40	0.24	2.9	• • •	• • •		ps
19565 + 3140	68.45	1.27	6.252	0.36	-0.48	8.0	20.5	• • •		ps
19576 + 2814	65.67	-0.74	17.410	0.33	-0.38	4.8	-56.8			ps
19598 + 3324	70.29	1.60	302.300	0.77	0.77	0.9				sf
20023 + 2855	66.79	-1.25	5.259	0.44	-0.13	8.4	-65.7			ps
20028 + 2903	66.96	-1.28	20.260	0.37	1.06	4.4				sf
20043 + 2653	65.32	-2.71	17.890	0.37	-0.32	4.7	-4.7			ps
20072 + 2710	65.91	-3.12	3.056	0.35	0.22	11.4				ps
20137 + 2838	67.93	-3.49	4.459	0.32	-0.62	9.5				ps
20187 + 4111	78.87	2.76	65.290	0.22	0.63	2.5				sf
20197 + 3722	75.84	0.41	423.700	0.46	0.78	0.9				sf?
20237 + 4003	78.48	1.33	2.202	0.42	0.55	13.2				ps
20249 + 3953	78.48	1.04	18.830	0.38	0.76	4.6				ppn?
20255 + 3932	78.26	0.74	5.300	0.13	0.25	8.2				ps
20288 + 3934	78.68	0.26	3.501	0.41	1.05	10.5				ps
20305 + 4010	79.34	0.34	2.461	0.48	1.35	12.1				ps
20319 + 3958	79.35	0.00	26.610	0.78	0.73	3.0				sf
20321 + 4112	80.35	0.72	5.227	0.73	1.18	7.1				sf?
20331 + 4024	79.83	0.10	7.379	0.69	0.55	6.1				no
20333 + 4102	80.36	0.44	22.850	0.52	1.22	3.9				sf?
20446 + 4613	85.70	2.03	3.250	0.52	1.09	10.3				sf?
20491 + 4236	83.42		54.810	0.10		2.4	-40.8			ps
21080 + 4758	89.64	0.17	7.490	0.59	0.67	6.5				sf
21329 + 5113		-0.33	2.477	0.19	1.41	12.5				no
23572 + 6702		4.94	4.307	0.18	1.20	9.4				
*										

ps: point sources, sf: star forming region with extended HII regions, sf?: possible star forming region, no: no clear counterpart, ppn?: extended sources with PPN-like morphology

Table 2. List of Detections.

		J = 1-0	v = 1			J = 1-0	v=2		
IRAS name	$V_{ m lsr}$	Ta	S	r.m.s.	$V_{ m lsr}$	$T_{\rm a}$	S	r.m.s.	Obs. date
	$({\rm km~s^{-1}})$	(K)	$({\rm K} \ {\rm km} \ {\rm s}^{-1})$	(K)	$({\rm km~s^{-1}})$	(K)	$(K \text{ km s}^{-1})$	(K)	(yymmdd.d)
17192-3206*	-189.6	0.147	0.227	0.046	-191.0	0.399	1.001	0.065	010322.2
$17286 - 3226^*$	-14.1	0.123	0.128	0.033	-12.3	0.199	0.384	0.044	010322.2
$17292 - 2727^*$				0.058	-67.8	0.477	1.753	0.071	010322.3
$17295 - 3321^*$	0.5	0.132	0.230	0.039	0.6	0.282	0.636	0.049	010322.3
$17317 - 3331^*$	9.1	2.426	5.516	0.102	7.9	7.025	20.441	0.129	010323.2
$17341 - 3529^*$	-60.6	0.212	0.487	0.066	-60.7	0.607	0.464	0.083	010322.2
17528 - 1503*				0.041	-62.7	0.268	0.793	0.055	010322.3
$17545 - 2512^*$	-126.1	2.299	8.126	0.056	-126.4	3.618	12.294	0.073	010322.3
18035 - 2114*	-37.6	0.387	0.920	0.061	-37.1	0.753	1.321	0.080	010320.3
$18080 - 2238^*$	54.4	0.279	0.271	0.053	56.6	0.416	1.509	0.064	010322.3
$18135 - 1456^*$	-4.6	0.735	2.395	0.052				0.063	010323.3
18152 - 0919*	26.3	0.520	1.453	0.061	26.4	0.694	1.370	0.075	010322.4
$18199 - 1442^*$				0.036	46.1	0.461	0.731	0.048	010320.3
18231 - 1112*	87.4	0.132	0.541	0.037	82.7	0.256	0.816	0.045	010323.3
$18242 - 0823^*$	150.4	0.124	0.174	0.036	149.6	0.271	0.469	0.049	010323.4
18251 - 1048*	85.4	0.207	0.783	0.042	86.8	0.565	2.311	0.054	010320.3
$18268 - 1117^*$				0.046	41.9	1.386	1.590	0.058	010323.4
$18348 - 0526^*$	27.2	17.172	26.853	0.109	27.2	34.386	65.085	0.140	010323.4
18432-0149*	68.5	1.089	3.491	0.105	67.9	1.924	8.283	0.131	010323.4
18450-0148*	20.1	0.235	1.127	0.049	20.0	0.208	0.360	0.059	010323.4
$18488 - 0107^*$	76.8	0.320	0.868	0.081	76.9	1.929	6.604	0.101	010322.4
$18498 - 0017^*$				0.069	60.1	0.824	2.449	0.094	010322.5
18509-0018*	38.6	0.738	0.572	0.111	38.3	1.258	3.255	0.140	010322.5
$18517 + 0037^*$	31.4	0.265	0.727	0.077	27.7	0.952	3.828	0.103	010321.4
18525+0210*	71.4	0.942	1.944	0.096	71.3	2.911	5.972	0.137	010321.4
18540+0302*	102.3	1.533	4.220	0.098	102.5	1.732	5.538	0.136	010321.4
18549 + 0208*	75.2	0.142	0.245	0.037	75.2	0.384	1.329	0.054	010321.3
18578 + 0831	49.3	0.313	0.504	0.056	49.7	0.343	0.671	0.064	000520.0
19006 + 0624	(-27.2)	(0.117)	(0.045)	0.035	-30.7	0.301	0.453	0.042	000520.1
19017+0608*	148.3	0.348	0.370	0.058	149.0	1.708	2.369	0.082	010321.4
19065 + 0832	52.0	0.250	[0.007]	0.079	52.3	1.329	3.025	0.091	000521.1
19067+0811	62.0	2.386	8.140	0.124	61.9	4.353	11.839	0.136	000521.1
19069+0916	30.0	0.608	0.895	0.082	30.1	0.611	1.185	0.099	000522.2
19071 + 0946				0.035	8.3	0.484	1.048	0.040	000522.2
19081+0322*	42.6	0.601	1.756	0.083	43.0	0.587	1.960	0.106	010323.5
19128+0910	(48.9)	(0.131)	(0.124)	0.040	50.4	0.300	0.694	0.045	000520.1
19175+1042	42.3	0.453	1.297	0.057	42.2	0.562	1.261	0.065	000523.2
19178 + 1206				0.032	41.3	0.405	0.580	0.058	010110.6
19178+1206 19183+1148	32.2	0.582	0.966	0.032 0.071	41.3	0.405 0.745	0.580 0.953	0.058 0.117	010110.6 010110.7

Table 2. (Continued)

		J = 1 - 0	v = 1			J = 1-0	v=2		
IRAS name	$V_{ m lsr}$	$T_{\rm a}$	S	r.m.s.	$V_{ m lsr}$	$T_{\rm a}$	S	r.m.s.	Obs. date
	$({\rm km~s^{-1}})$	(K)	$(K \text{ km s}^{-1})$	(K)	$(\mathrm{km}\ \mathrm{s}^{-1})$	(K)	$(K \text{ km s}^{-1})$	(K)	(yymmdd.d)
19188 + 1057	-23.9	0.263	0.662	0.048	-24.0	0.485	1.532	0.057	000522.3
19200 + 1536	64.2	0.179	0.422	0.041	61.8	0.214	0.633	0.051	000522.3
19254 + 1631	3.2	1.775	7.519	0.095	3.0	2.197	9.960	0.111	000523.3
19283 + 1944	28.0	0.663	2.587	0.079	27.6	0.640	2.549	0.095	000522.4
19295 + 2228	-73.2	0.706	1.455	0.076	-72.8	1.268	3.292	0.089	000521.2
19312+1950**	25.4	0.131	0.731	0.024	26.8	0.118	0.499	0.022	000531.2
19440 + 2251	-9.6	0.304	0.781	0.056	-9.1	0.472	0.612	0.070	000520.3
19565 + 3140	20.7	0.556	1.887	0.074	20.3	0.937	3.728	0.089	000520.3
19576 + 2814				0.076	-56.8	0.684	1.915	0.089	000520.4
20023 + 2855	(-66.2)	(0.191)	(0.285)	0.064	-65.2	0.678	1.614	0.080	000520.4
20043 + 2653	-3.9	0.785	2.243	0.088	-5.5	1.186	5.904	0.099	000521.4
20491+4236	-40.8	2.045	6.321	0.129	-40.8	1.502	4.504	0.157	000420.5

^{*:} Sources observed at MSX position (see text).

^{**:} An oject reported by Nakashima, Deguchi (2000).

^{():} The values in parentheses are for dubious detections.

^{[]:} This value is unexpectedly low because of artificial concave at just right side of the maser.

Table 3. List of non-detections.

IRAS name	r.m.s. $(J = 1-0, v = 1)$	r.m.s. $(J = 1-0, v = 2)$	Obs. date
	(K)	(K)	(yymmdd.d)
17271-3309*	0.078	0.065	010323.2
18008-2419*	0.072	0.059	010323.2
18016-2743*	0.062	0.050	010320.3
18016-2540*	0.070	0.056	010322.3
18042-2131*	0.059	0.044	010320.3
$18071 - 1727^*$	0.068	0.053	010323.2
18092-1742*	0.068	0.055	010322.4
18112-1801*	0.067	0.053	010323.2
$18125 - 1631^*$	0.064	0.053	010323.3
18171-1603*	0.060	0.048	010323.3
18184-1449*	0.059	0.046	010323.3
18196-1331*	0.060	0.046	010323.3
18223-1243*	0.058	0.046	010323.3
18262-1233*	0.065	0.051	010323.4
18321-0820*	0.063	0.046	010320.4
18354-0638*	0.076	0.056	010322.4
18418-0415*	0.076	0.060	010322.4
18434-0308*	0.080	0.063	010322.4
18511+0146*	0.084	0.061	010321.5
18529+0210*	0.077	0.056	010321.4
18542+0114*	0.062	0.046	010321.4
18587 + 0521*	0.089	0.072	010323.5
19008+0530*	0.070	0.050	010321.3
19011 + 0852	0.039	0.032	000522.1
19011 + 1049	0.058	0.049	000520.0
19025 + 0613	0.046	0.047	000524.0
19026 + 0614	0.046	0.034	010319.4
19045 + 0518*	0.085	0.063	010321.5
19048 + 0914	0.044	0.031	010320.2
19057 + 1002	0.051	0.036	010321.3
19069 + 1335	0.045	0.056	000522.4
19077 + 0839	0.049	0.043	000520.0
19080 + 0748	0.058	0.050	000522.2
19085 + 0755	0.061	0.051	000522.2
19089 + 1542	0.048	0.041	000521.1
19108+0901	0.059	0.044	010321.3
19112 + 1220	0.045	0.036	000521.2
19123+1139	0.063	0.051	000522.2
19134+2131	0.045	0.037	000520.1
19143+1427	0.052	0.037	010321.4

Table 3. (Continued)

IRAS name	r.m.s. $(J = 1-0, v = 1)$	r.m.s. $(J = 1-0, v = 2)$	Obs. date
	(K)	(K)	(yymmdd.d)
19167+1313	0.060	0.048	000522.3
19171+1119	0.063	0.050	000522.3
19177+1333	0.043	0.035	000521.2
19195+1650	0.052	0.062	000522.3
19199 + 2100	0.074	0.063	000522.3
19199 + 2100	0.064	0.078	000522.3
19200 + 2101	0.056	0.046	000523.2
19200 + 1035	0.062	0.037	010110.7
19205 + 1447	0.056	0.047	000523.2
19207 + 1348	0.056	0.046	000523.2
19207 + 1346	0.057	0.050	000523.2
19211 + 1432	0.059	0.048	000523.3
19223 + 1359	0.058	0.048	000523.3
19226 + 1401	0.042	0.033	000520.1
19228+1403	0.061	0.054	000523.3
19244+1115	0.115	0.097	000420.4
19270 + 1550	0.066	0.053	000523.3
19281 + 2308	0.044	0.036	000521.2
19294 + 1649	0.064	0.058	000523.3
19295 + 1637	0.068	0.055	000523.3
19310 + 1745	0.071	0.063	000523.3
19319 + 2214	0.044	0.036	000521.3
19327 + 3024	0.060	0.052	000521.3
19332 + 2028	0.043	0.036	000520.2
19340 + 2016	0.066	0.054	000521.3
19341 + 2038	0.066	0.053	000523.4
19344 + 2457	0.045	0.038	000520.2
19352 + 2030	0.079	0.064	000521.3
19365 + 1023	0.053	0.039	010321.4
19374 + 1626	0.059	0.052	000521.3
19421 + 2507	0.045	0.037	000520.3
19473 + 2638	0.068	0.062	000523.4
19479 + 2620	0.048	0.041	000520.3
19520 + 2759	0.061	0.052	000521.3
19598 + 3324	0.084	0.080	000527.4
20028 + 2903	0.130	0.106	000520.4
20072 + 2710	0.056	0.044	000520.3
20137 + 2838	0.095	0.080	000521.4
20187 + 4111	0.068	0.059	000420.5
20197 + 3722	0.082	0.071	000427.5
20237+4003	0.076	0.116	000530.3

Table 3. (Continued)

IRAS name	r.m.s. $(J = 1-0, v = 1)$	r.m.s. $(J = 1-0, v = 2)$	Obs. date
	(K)	(K)	(yymmdd.d)
20249 + 3953	0.113	0.098	000426.5
20255 + 3932	0.056	0.068	000530.4
20288 + 3934	0.054	0.064	000530.3
20305 + 4010	0.060	0.067	000530.4
20319 + 3958	0.058	0.066	000529.4
20321 + 4112	0.079	0.105	000530.3
20331 + 4024	0.072	0.080	000529.4
20333 + 4102	0.079	0.063	000529.4
20446 + 4613	0.077	0.085	000530.3
21080 + 4758	0.073	0.065	000527.4
21329 + 5113	0.062	0.110	000531.3
23572 + 6702	0.051	0.057	000531.4

^{*:} Sources observed at MSX positions.

Table 4. H_2O detections.

IRAS name	ΔV	V_{C}	$V_{\rm p}$	T_{p}	Flux	r.m.s.	Obs. date
	$({\rm km~s^{-1}})$	$({\rm km~s^{-1}})$	(K)	(K)	$({\rm K~km~s^{-1}})$	(K)	(yymmdd.d)
19067+0811	27.8	62.8	76.7	1.243	8.482	0.053	000528.2
			48.9	0.897	7.239		
19069 + 0916	36.4	-7.5	10.7	2.328	35.166	0.049	000528.2
			-25.7	1.675	8.801		
19312 + 1950		17.4	17.4	2.339	7.455	0.062	000601.0

Table 5. H_2O non-detections.

IRAS name	r.m.s.	Obs. date
	(K)	(yymmdd.d)
18171-1603	0.055	000528.1
18578 + 0831	0.080	000528.2
19006 + 0624	0.081	000528.2
19065 + 0832	0.067	000528.2
19071 + 0946	0.077	000528.2
19128 + 0910	0.081	000528.3
19175 + 1042	0.080	000528.3
19178 + 1206	0.023	010210.0
19183 + 1148	0.023	010210.0
19188 + 1057	0.096	000528.3
19200 + 1536	0.101	000528.3
19254 + 1631	0.066	000531.9
19283 + 1944	0.052	000601.0
19295 + 2228	0.073	000601.0
19309 + 2646	0.033	010210.0
19440 + 2251	0.090	000528.3
19565 + 3140	0.088	000528.3
19576 + 2814	0.087	000528.3
20023 + 2855	0.073	000601.0
20043 + 2653	0.145	000528.3

Table 6. detected masers.

IRAS name	OI	H (1612 N	MHz)	E	I ₂ O	SiO, $J = 1$	1-0, v=1,2
	$V_{ m lsr}$	ΔV (km s ⁻¹)	Ref.	$V_{ m lsr}$	Ref.	$V_{ m lsr}$	Ref.
17192-3206	(km s)	(km s)		(KIII S)		-190.3	1
17286 - 3226	-12.5	30.5	11, 13			-13.2	1
17292-2727	-67.2	35.2	4, 13			-68.3	1
17295-3321	0.6	30.1	11, 12, 13			0.6	1
17317-3331	8.6	29.2	4, 11, 12			8.5	1, 10
17341-3529	0.0	20.2	1, 11, 12			-60.6	1
17528-1503	-67.5	29.0	12			-62.7	1
17545 - 2512	-123.5	45.2	4, 11, 12			-126.2	1
18016-2743	72.5	22.0	4, 11, 13			120.2	-
18035-2114			1, 11, 10			-37.3	1
18042-2131	193.3	33.6	11			31.3	-
18071-1727	25.9	16.9	4, 12				
18080-2238	55.0	33.6	11, 13			55.5	1
18092 - 1742	138.5	27.0	12				_
18135-1456	-1.15	28.2	4, 12	У	7	-4.9	1, 10
18152-0919	26.7	28.2	4, 12	J		26.3	1
18196-1331	31.0	18.0	12				
18199-1442	40.6	7.7	13			46.0	1
18231-1112						85.0	1
18242-0823						150.0	1
18251-1048	91.0	40.0	12			86.1	1
18268-1117	42.5	34.5	4, 13			43.4	1
18348-0526	27.8	27.9	4, 12, 13	35.0	2	27.2	1, 10
18432-0149	67.1	35.1	4, 12, 13	55.0	2	68.2	1
18434-0308	76.2	41.0	13				
18450-0148	34.0	14.0	12			20.1	1
18488-0107	75.8	40.9	4, 12			76.9	1
18498-0017	60.7	30.8	12	48.0	2, 7	60.1	1
18509-0018						38.4	1
18517 + 0037	28.0	34.2	4, 13	28.4	6	29.6	1
18525 + 0210	70.0	38.6	13, 4	70.7	6	71.3	1
18540 + 0302	102.9	37.4	12, 13	85.8	2, 6	102.4	1
18549 + 0208	78.6	27.4	4, 13	у	6	75.2	1
18578 + 0831	49.3	29.0	13	у	6	49.5	1
19006 + 0624	-29.9	30.4	4, 13			-28.9	1
19017 + 0608	149.6	28.5	4, 13	У	6	148.7	1, 8
19065 + 0832	53.1	35.4	4, 12			52.2	1
19067 + 0811	59.5	32.5	4, 12	У	6	62.0	1,10,
							8

Table 6. (Continued)

IRAS name	OH (1612 M		MHz)	Н	-2O	SiO, $J =$	1-0, v=1,2
	$V_{ m lsr}$	ΔV (km s ⁻¹)	Ref.	$V_{ m lsr}$	Ref.	$V_{ m lsr}$	Ref.
19069+0916	31.7	43.6	5	26.7	2, 6	30.1	1
19071 + 0946	9.1	23.2	4, 12	У	6, 7	8.3	1
19081 + 0322	42.2	32.0	4, 13	43.0	6	42.8	1
19085 + 0755	77.3	38.9	4, 13	78.1	6		
19112 + 1220	62.2	33.1	4				
19128 + 0910	52.4	25.3	12, 13			49.7	1
19134 + 2131				-17.2	2		
19175 + 1042				у	6	42.3	1
19178 + 1206						41.3	1
19183 + 1148	35.5	31.8	13			32.7	1
19188 + 1057	-21.2	27.2	13			-24.0	1
19199 + 2100	56.3	26.2	13				
19200 + 2101	55.3	26.7	12				
19200 + 1536	61.0	26.2	4, 12, 13			63.0	1
19244 + 1115	76.4	61.4	12, 13				
19254 + 1631	1.4	37.2	4, 12			3.1	1
19283 + 1944	27.0	28.0	12			27.8	1
19295 + 2228	-74.5	25.0	12			-73.0	1
19312 + 1950						26.1	1
19319 + 2214	20.6	16.3	4	14.2	6		
19344 + 2457	16.1	22.9	13				
19352 + 2030	0.5	7.0	12				
19374 + 1626	-28.6	26.1	4, 13				
19440 + 2251	-7.58	34.9	4, 12			-9.4	1
19565 + 3140				У	6	20.5	1
19576 + 2814	-58.87	21.5	4, 9, 12			-56.8	1
19598 + 3324				-19	2		
20023 + 2855	-63.65	25.6	4, 12			-65.7	1
20043 + 2653	-4.56	26.4	4, 9			-4.7	1
20072 + 2710	n		3				
20137 + 2838				-67.9	2, 6		
20491 + 4236	-39	36.0	12			-40.8	1

References: 1—this paper, 2—Cesaroni et al. (1988), 3—Chengalur et al. (1993),

⁴—David et al. (1993), 5—Eder et al. (1988), 6—Engels, Lewis (1996),

^{7—}Engels et al. (1986), 8—Jewell et al. (1991), 9—Likkel (1989),

¹⁰—Nyman et al. (1993), 11—Sevenster et al. (1997), 12—te Lintel Hekkert et al. (1989), 13—te Lintel Hekkert $\,$ 1991a.

References

Barvainis, R., & Clemens, D. P. 1984, AJ, 89, 1833

Blöcker, T. 1995, A&A, 297, 727

Bronfman, L., Nyman, L. -Å., & May, J. 1996, A&AS, 115, 81

Cesaroni, R., Palagi, F., Felli, M., Catarzi, M., Comoretto, G., Di Franco, S., Giovanardi, C., & Palla, F. 1988, A&AS, 76, 445

Chengalur, J. N., Lewis, B. M., Eder, J., & Terzian, Y. 1993, ApJS, 89, 189

Dame, T. M., Hartmann, D., & Thaddeus, P. 2001, ApJ, 547, 792

David, P., Le Squeren, A. M., & Sivagnanam, P. 1993, A&A, 277, 453

Deguchi, S., Fujii, T., Izumiura, H., Kameya, O., Nakada, Y., & Nakashima, J. 2000a, ApJS, 130, 351

Deguchi, S., Fujii, T., Kameya, O., Nakada, Y., Nakashima, J., Ootsubo, T., & Ukita, N. 2000b, ApJS, 128, 571

Deguchi, S., Fujii, T., Matsumoto, S., Nakashima, J., & Wood, P. R. 2001a, PASJ, 53, 293

Deguchi, S., Nakashima, J., & Balasubramanyam, R. 2001b, PASJ, 53, 305

Eder, J., Lewis, B. M., & Terzian, Y. 1988, ApJS, 66, 183

Elitzur, M. 1992, in Astronomical Masers (Kluwer Academic Phlishers) p. 280

Engels, D. 2002, A&A, 388, 252

Engels, D., & Lewis, B. M. 1996, A&AS, 116, 117

Engels, D., Schmid-Burgk, J., & Walmsley, C. M. 1986, A&A, 167, 129

Frail, D. A., & Beasley, A. J. 1994, A&A, 290, 796

Fuente, A., Martín-Pintado, J., Alcolea, J., & Barcia, A. 1989, A&A, 223, 321

Fujii, T., Nakada, Y., & Parthasarathy, M. 2002, A&A, 385, 884

Fullmer, L., & Lonsdale, C. 1989, Cataloged Galaxies & Quasers Observed in the IRAS Survey (Pasadena: JPL)

Geballe, T. R., & Oka, T. 1996, Nature, 384, 334

Gezari, D. Y., Backman, D. E., & Werner, M. W. 1998, ApJ, 509, 283

Gómez, Y., Rodríguez, L. F., Contreras, M. E., Moran, J. M. 1994, Rev. Mex. Astron. Astrofis. 28, 97

Habing, H. J. 1996, A&Ap Rev. 7, 97

Hasegawa, T., Morita, K., Okumura, S., Kaifu, N., Suzuki, H., Ohishi, M., Hayashi, M., & Ukita, N. 1986, in Masers, Molecules and Mass Outflows in Star Forming Regions, ed Haschick, A. D. (Westford: Haystack Observatory)

Harrington, J. P., Lame, N. J., White, S. M., & Borkowski, K. J. 1997, AJ, 113, 2147

Hillenbrand, L. A., Meyer, M. R., Strom, S. E., & Skrutskie, M. F. 1995, AJ, 109, 280

Imai, H., Obara, K., Diamond, P. J., Omodaka, T., & Sasao, T. 2002, Nature 417, 829

Imai, H., Deguchi, S., & Miyoshi, M. 1999, PASJ, 51, 587

Izumiura, H., Deguchi, S., Fujii, T., Kameya, O., Matsumoto, S., Nakada, Y., Ootsubo, T., & Ukita, N. 1999, ApJS, 125, 257

Izumiura, H., Deguchi, S., Hashimoto, O., Nakada, Y., Onaka, T., Ono, T., Ukita, N., & Yamamura, I. 1994, ApJ, 437, 419

Izumiura, H., Deguchi, S., Hashimoto, O., Nakada, Y., Onaka, T., Ono, T., Ukita, N., & Yamamura, I. 1995b, ApJ, 453, 837

Jewell, P. R., Bartla, W., Walmsley, C. M., & Wilson, T. L. 1984, A&A, 130, L1

Jewell, P. R., Snyder, L. E., Walmsley, C. M., Wilson, T. L., & Gensheimer, P. D. 1991, A&A, 242, 211

Jiang, B. W., Deguchi, S., Izumiura, H., Nakada, Y., Yamamura, I., 1995, PASJ, 47, 815

Kastner, J. H., Weintraub, D. A., & Aspin, C. 1992, ApJ, 389, 357

Kawamura, J., & Masson, C. 1996, ApJ, 461, 282

Likkel, L. 1989, ApJ, 344, 350

Likkel, L., Forveille, T., Omont, A., & Morris, M. 1991, A&A, 246, 153

Likkel, L., Morris, M., & Maddalena, R. J. 1992, A&A, 256, 581

Likkel, L., Omont, A., Morris, M., & Forveille, T. 1987, A&A, 173, L11

Meeus, G., Waters, L. B. F. M., Bouwman, J., van den Ancker, M. E., Waelkens, C., & Malfait, K. 2001, A&A, 365, 476

Meixner, M., Ueta, T., Dayal, A., Hora, J. L., Fazio, G., Hrivnak, B, J., Skinner, C. J., Hoffmann, W. F., & Deutsch, L. K. 1999, ApJS, 122, 221

Minchin, N. R., Hough, J. H., Burton, M. G., & Yamashima, T. 1991, MNRAS, 251, 522

Morita, K.-I., Hasegawa, T., Ukita, N., Okumura, S. K., & Ishiguro, M. 1992, PASJ, 44, 373

Morris, M., Guilloteau, S., Lucas, R., & Omont, A. 1987, ApJ, 321, 888

Nakada, Y., Onaka, T., Yamamura, I., Deguchi, S., Ukita, N., & Izumiura, H. 1993, PASJ, 45, 179

Nakashima, J., & Deguchi, S. 2000, PASJ, 52, L43

Nakashima, J., & Deguchi, S. 2002, PASJ, (submitted to PASJ)

Nakashima, J., Deguchi, S., Fujii, T., Izumiura, H., Kameya, O., & Nakada, Y. 2002, ApJ,(submitted to ApJ)

Nakashima, J., Jiang, B. W., Deguchi, S., Sadakane, K., & Nakada, Y. 2000, PASJ, 52, 275

Nyman, L.-Å., Hall, P. J., & Le Bertre, T. 1993, A&A, 280, 551

Nyman, L.-Å., Hall, P. J., & Olofsson, H. 1998, A&AS, 127, 185

Nyman, L.-Å., & Olofsson, H. 1986, A&A, 158, 67

Okamoto, Y. K., Kataza, H., Yamashita, T., Miyata, T., Onaka, T., 2001, ApJ, 553, 254

Olofsson, H., Rydbeck, O. E. H., Lane, A. P., & Predmore, C. R. 1981, ApJ, 247, L81

Olofsson, H., Rydbeck, O. E. H., & Nyman, L.-Å. 1985, A&A, 150, 169

Onaka, T., Yamamura, I., Jong, T. D., Tanabé, T., Hashimoto, O., Izumiura, H. 1997, Ap&SS 255, 331

Pashchenko, M. I., & Le Skeren, A. M. 1994, Astronomy Letters, 20, 69

Price, S. D., Egan, M. P., Shipman, R. F., Tedesco, E. F., Cohen, M., Walker, R. G., & Moshir, M. 1997, BAAS, 29, 1294

Renzini, A. 1981, in Physical Process in Red Giants, ed. I. Iben Jr & A. Renzini (Dordrecht: Reidel), 431

Schwartz, P. R., Waak, J. A., & Bologna, J. M. 1979, AJ, 84, 1349

Sevenster, M. N., Chapman, J. M., Habing, H. J., Killeen, N. E. B., & Lindqvist, M. 1997, A&AS, 122, 79

Shiki, S., Ohishi, M., & Deguchi, S. 1997, ApJ, 478, 206

Silva, A. M., Azcarate, I.N., Poppel, W.G. L., & Likkel, L.1993, A&A, 275, 510

Spencer, J. H., Winnberg, A., Olnon, F. M., Schwartz, P. R., Matthews, H. E., & Downes, D. 1981, AJ, 86, 392

Suh, K.-W., & Jones, T. J. 1997, ApJ, 479, 918

Stuers, M., & Zealey, W. 1991, Pub. Astron. Soc. Australia, 9, 140

Taylor, J. H., & Cordes, J. M. 1993, ApJ, 411, 674

te Lintel Hekkert, P. 1991a, A&A, 248, 209

te Lintel Hekkert, P., Caswell, J. L., Habing, H. J., Haynes, R. F., & Norris, R. P. 1991b, A&AS, 90, 327

te Lintel Hekkert, P., Versteege-Hensel, H. A., Habing, H. J., & Wiertz, M. 1989, A&AS, 78, 399

Thé, P. S., de Winter, D., & Pérez, M. R. 1994, A&AS, 104, 315

van der Veen, W. E. C. J., & Breukers, R. J. L. H. 1989, A&A, 213, 133

van der Veen, W. E. C. J., & Habing, H. J. 1988, A&A, 194, 125

van Hoof, P. A. M., Oudmaijer, R. D., Waters, L. B. F. M. 1997, MNRAS, 289, 371

van Loon, J. Th., Zijlstra, A. A., Kaper, L., Gilmore, G. F., Loup, C., & Blommaert, J. A. D. L. 2001, A&A, 368, 239

Vassiliadis, E., Wood, P. R. 1993, ApJ, 413, 641

Watt, S., & Mundy, L. G. 1999, ApJS, 125, 143

Wilking, B. A., Blackwell, J. H., & Mundy L. G. 1990, AJ, 100, 758

Wilking, B. A., Mundy, L. G., Blackwell, J. H., & Howe, J. E. 1989, ApJ, 345, 257

Yamamura, I., Onaka, T., Kamijo, F., Deguchi, S., Ukita, N. 1996, ApJ, 465, 926

Yang, J., Jiang, Z., Wang, M., Ju, B., & Wang, H. 2002, ApJ, 141, 157